



Thermal Fluctuations and Bending of Light in Euler-Heisenberg Nonlinear Electrodynamics

H. Gürsel ^{*}, M. Mangut [†] and E. Sucu [‡]
*Department of Physics, Eastern Mediterranean University,
Famagusta, 99628 North Cyprus via Mersin 10, Turkey*

This work mainly focuses on the nonlinear Euler-Heisenberg theory and its applications from various aspects. Firstly, thermodynamic parameters such as the Hawking temperature, the heat capacity, enthalpy and Gibbs free energy are analytically determined via Smarr's formula for a four-dimensional Einstein-Euler-Heisenberg black hole by taking the Hawking-Bekenstein entropy as the basis. The results are also demonstrated graphically for certain Euler-Heisenberg and electric charge parameters, which are in turn used for making further comments on the stability and possible critical points of the concerned black hole. The thermodynamic analyses are then repeated for two distinct cases in which entropy is subject to a *logarithmic* and an *exponential* correction, respectively. Our analyses have shown that if one desires to investigate possible phase transitions of the concerned black hole, there exists a unique upper limit for the value the nonlinear Euler-Heisenberg parameter can take for each electric charge parameter, whose value is determined to four significant figures, when possible. For both the classical Hawking-Bekenstein and the logarithmically corrected entropies, these upper limits are found as $\mu < 9.143$, $\mu < 36.57$, $\mu < 82.28$ and $\mu < 146.3$ for $q = 2, 4, 6$ and 8 , respectively. For the exponentially corrected case, however, no upper limits could be determined for the NED parameter, as the plots consisted of vertical discrete lines in the positive domain rather than smooth functions with reversed trends. Finally, the one-sided bending angle and the gravitational redshift of light are determined in the vicinity of astronomical structures obeying the nonlinear Euler-Heisenberg model. The results obtained are applied to three electrically charged, compact stars: Vela X-1, SAXJ1808.4-3658 and 4U1820-30. During the astrophysical applications, the spacetime background is assumed to obey the Euler-Heisenberg model due to the presence of strong electromagnetic fields. Consequently, quantum corrections caused by such strong interactions are ensured to be involved within the results presented.

I. INTRODUCTION

Toward the end of the mid-19th century, the theory of classical electrodynamics was constructed by James Clerk Maxwell [1], through which Faraday's experimental discoveries were explained via the unification of electricity and magnetism. Maxwell's equations combined with preceding and subsequent work carried out by numerous scientists eventually led to the establishment of classical field theory. However, despite all the beauty and predictions offered by the theory, Maxwell's equations seemed to remain insufficient in explaining the Sauter-Schwinger effect [2, 3] observed almost a century later, which briefly refers to the formation of particle-antiparticle pairs in vacuum in the presence of a strong electric field. This phenomenon can be considered as an extension of Dirac's relativistic quantum theory of the electron [4] giving birth to further pioneering developments in both theoretical and experimental physics.

In addition to the lack of the theoretical understanding behind the Sauter-Schwinger effect, when the electric field produced by a point electric charge was examined, the self-interaction was found to be not well defined, suggesting that classical electrodynamics required corrections. To overcome the point charge singularity, a nonlinear modification was carried out by Born and Infeld [5]. Although the implementation of this modification resolved the singularity issue, the Born-Infeld model is still classified as a purely classical theory, since no quantum-mechanical principles are involved. Some studies on the Born-Infeld theory can be found in [5–11]. The inclusion of quantum mechanics in the theory of electrodynamics took place with the work of Euler and Heisenberg [12] approximately two years after the proposal of the Born-Infeld model. Euler-Heisenberg nonlinear electrodynamics (NED) is currently considered as a promising model to refer to for describing the quantum corrections caused by strong electromagnetic fields. This model predicts that the vacuum will exhibit nonlinear properties such as vacuum polarisation and photon-photon scattering once exposed to strong electromagnetic fields. Furthermore, the integration of quantum corrections into

*Electronic address: huriye.gursel@emu.edu.tr

†Electronic address: mert.mangut@emu.edu.tr

‡Electronic address: erdemsc07@gmail.com

the field of electrodynamics enables one to study the nonlinear terms that appear in the mathematical analysis of astrophysical phenomena involving strong electromagnetic fields, such as those experienced by neutron stars [13, 14].

Recent studies have shown interesting applications of Euler-Heisenberg NED in various fields. For instance, if one wishes to inspect the role of quantum corrections caused by strong electromagnetic fields in the general theory of relativity, picking the Einstein-Euler-Heisenberg black hole as the target object of concern would be a wise choice. In this case, the relevant Lagrangian density can be written as follows.

$$\mathcal{L}_{EEH} = \underbrace{-\frac{1}{4}F_{\mu\nu}F^{\mu\nu}}_{\text{Maxwell term}} + \underbrace{\frac{\bar{\alpha}^2}{90m_e^2} \left[(F_{\mu\nu}F^{\mu\nu})^2 + \frac{7}{4} (F_{\mu\nu}\tilde{F}^{\mu\nu})^2 \right]}_{\text{Euler-Heisenberg term}}. \quad (1)$$

Here, $F_{\mu\nu}$ and $\tilde{F}_{\mu\nu}$ represent the normal and dual electromagnetic field strengths, whereas m_e and $\bar{\alpha}$ stand for the rest mass of the electron and the fine structure constant, respectively.

In [15], birefringence and quasinormal modes of Einstein-Euler-Heisenberg black holes are studied in the eikonal approximation; whereas in [16], the thermodynamic properties and phase transitions are examined with the inclusion of cosmological constant in the Euler-Heisenberg theory. Furthermore, a NED theory whose action involves Maxwell, weak Euler-Heisenberg and strong electromagnetic terms is analysed for the electrostatic case with the aim of investigating the corrections of Coulomb's law of a point charge in [17]. In this regard, numerical methods (one of which can be found in [18]) have been constructed to solve NED equations of Euler-Heisenberg weak field expansion, and consequently, simulations of nonlinear quantum vacuum are established. In another study [19], detailed analyses are carried out on the corrections of Coulomb's law and charged black hole solutions in two-parameter Euler-Heisenberg NED model.

Black hole thermodynamics is considered as a prominent theoretical framework that combines laws of thermodynamics with principles of general relativity and quantum mechanics[20–23]. In addition, the interconnection between the thermodynamic concepts and the geometrical properties of black holes play a vital role in the pursuit of developing a quantum theory of gravity. The study of concepts such as Bekenstein-Hawking entropy [24–26] and Hawking radiation [27] raises intriguing questions about the information content and the thermodynamic future of the universe. Some examples of such discussions can be found in [28, 29]. It is also worthwhile noting that the merging of thermodynamics and general relativity enables one to carry out the stability analysis of solutions of Einstein's equations by examining the potentials of the concerned thermal systems, as well as the evaluating thermodynamic parameters such as the heat capacity (C), a critical term in the determination of the overall stability (negative C indicating thermodynamic instability [30]), the enthalpy (H), the internal (E), Helmholtz (F) and Gibbs (G) free energies[31]. One can also use the stability analysis to assess phase transitions, since the divergence of C is usually an indicator of a critical point.

To evaluate the thermodynamic parameters, one would need to have a convenient expression for the entropy of the black hole structure of concern. With the development of principles of AdS/CFT correspondence, loop quantum gravity, string theory, and other frameworks, the Bekenstein-Hawking entropy has been receiving various modifications over the years. For some examples, one can refer to [32–36]. By combining the discussions of statistical mechanics with the models mentioned above, the corrected entropy of a black hole can be written as [37]

$$S = S_0 + \xi \ln f_1(S_0) + \frac{\gamma}{S_0} + \eta e^{-S_0}, \quad (2)$$

where S_0 is the Bekenstein-Hawking entropy such that $S_0 = \mathcal{A}/4l_P^2$. Here, \mathcal{A} refers to the horizon area and l_P is the Planck length. The logarithmic and the inverse area terms arise due to small stable fluctuations around equilibrium [33], whereas the exponential contribution is treated as a non-perturbative quantum correction [38]. Although there exist a large number of studies in the literature on the derivation and implications of the logarithmic and inverse area terms[39–53], the exponential correction has less thoroughly been investigated (see[36, 54] for some examples).

In this study, the thermodynamic potential of an Einstein-Euler-Heisenberg black hole will be determined by considering the logarithmic and exponential corrections mentioned in (2) separately. Doing so allows one to examine two distinct black hole states, the small- and large-horizon regimes, independently. Then, for each case, the relevant thermodynamic parameters will be analytically evaluated and stability analyses will be carried out accordingly. For small horizons, the horizon area obeys $A \sim l_p^2$, which in turn makes the corrected entropy reduce to [54]

$$S \sim S_0 + \eta e^{-S_0}. \quad (3)$$

In [54], Chatterjee and Ghosh derived a general equation for the entropy of any black hole with an isolated horizon in the case where the horizon area is small. Rather than using the tools of string theory and loop quantum gravity, the authors based their discussions on the horizon geometry. The entropy derived with the concerned method is consistent with (3).

In contrast, if the horizon area is relatively large, the entropy becomes [45]

$$S \sim S_0 + \xi \ln f_1(S_0). \quad (4)$$

An entropy corrected in this form is considered for charged anti-de Sitter [55], Horava-Lifshitz [56], singly spinning Kerr-AdS [57] and symmergent [58] black holes. Furthermore, the effect of these small fluctuations around equilibrium on thermodynamic parameters is studied for $\mathcal{F}(R, \mathcal{G})$ gravity black holes with constant topological Euler density in NED [59], Kerr-Newman-AdS and Reissner-Nordström-AdS black holes [60].

Gravitational lensing, a strong observational tool in testing the validity of models constructed based on Einstein's theory of general relativity, can also be used to assess models emerging out of NED[61–64]. In the majority of the cases, the mathematical complexity of NED equations yields black hole solutions including non-trivial functions, which may eventually give rise to difficulties when it comes to determining the associated lensing angle theoretically. Such challenges can be handled by using the generalisation of the inner product to curved spacetimes proposed by Rindler and Ishak [65]. This method has been shown to cause nonlinear modifications to the purely electrical solutions of Einstein-Power-Maxwell NED theory, as well as to the purely electrical and purely magnetic solutions of the non-linear Kruglov model [64, 66].

One of the most significant applications of the Rindler-Ishak method is the determination of the gravitational lensing angle around compact astronomical objects. In this paper, the gravitational lensing angles in the vicinity of VelaX-1, SAXJ1808.4-3658 and 4U1820.30 will be evaluated. During our calculations, the numerical values of the mass, charge and radius of the concerned objects will be taken from [67]. Since all of the objects specified above include strong electromagnetic fields, the metric of choice will be determined based on the Euler-Heisenberg NED theory, which will enable us to use our theoretical results in observational applications. The method of Rindler and Ishak is generalised in [68] for rotating metrics and its application showed indications of cosmic voids in rotating Bertotti-Robinson spacetimes. Moreover, the effect of Lorentz symmetry breaking on the lensing angle is analytically analysed for rotating Bumblebee black holes [69] and the same methodology is used to calculate the lensing angle in the vicinity of a Kerr-Newman-AdS black hole, together with some applications [70].

This study consists of five sections. In Section II, the physical properties of the Einstein-Euler-Heisenberg black hole will be provided briefly, which will then be followed by a detailed analysis of its thermodynamic characteristics constituting Section III. The analytical solutions obtained will be supported by graphical illustrations for further analysis. Section IV will focus on the astrophysical applications of the Euler-Heisenberg NED theory by examining gravitational lensing and gravitational redshift. Finally, conclusive remarks will be presented in the last section.

II. PHYSICAL PROPERTIES OF EINSTEIN-EULER-HEISENBERG BLACK HOLE

In four-dimensional spacetime, the general action integral of the Einstein-Hilbert theory with Euler-Heisenberg NED is provided by

$$\mathcal{I} = \frac{1}{4\pi} \int d^4x \sqrt{-g} \left[\frac{\mathcal{R}}{4} - \mathcal{L}_{EEH} \right], \quad (5)$$

in which R is the Ricci scalar, g is the metric tensor determinant, and \mathcal{L}_{EEH} is the Lagrangian density stated in (1). The static spherically symmetric black hole solution of the Euler-Heisenberg theory can be expressed as [15, 71]

$$ds^2 = f(r)dt^2 - \frac{dr^2}{f(r)} - r^2 (d\theta^2 + \sin^2(\theta)d\phi^2), \quad (6)$$

where

$$f(r) = 1 - \frac{2M}{r} + \frac{q^2}{r^2} \left(1 - \frac{\mu q^2}{20r^4}\right), \quad (7)$$

such that M and q represent the mass and the electric charge of the black hole, respectively. Also, note that $\mu \equiv \frac{2\alpha^2}{45m_e^2}$ stands for the nonlinear Euler-Heisenberg parameter, and for $\mu \rightarrow 0$, the solution reduces to the Reissner–Nordström structure.

For Einstein-Euler-Heisenberg black holes, the Hawking temperature is

$$T_H = \frac{1}{4\pi} f'(r)|_{r=r_h} = \frac{1}{4\pi r_h} - \frac{q^2}{4\pi r_h^3} + \frac{\mu q^4}{16\pi r_h^7}, \quad (8)$$

where, r_h represents the radius of the event horizon. To find the real positive roots, one can set $f(r_h) = 0$ which leads to

$$r_h^6 - 2r_h^5 + q^2 r_h^4 - \frac{\mu q^4}{20} = 0. \quad (9)$$

The dimensionless parameters $q \rightarrow q/M$ and $\mu \rightarrow \mu/M^2$ are introduced in [72]. For the cases when the conditions $\mu/M^2 \leq 50/81$ and $q^2/M^2 \leq 25/24$ are satisfied, the extreme black hole admits one outer horizon and two inner horizons. For further details on these constraints, one may check [15, 73].

III. THERMODYNAMIC CHARACTERISTICS OF EINSTEIN-EULER-HEISENBERG BLACK HOLE

In this section, after the examination of the standard thermodynamic structure of the Einstein-Euler-Heisenberg black hole via Smarr's formula, the associated thermal fluctuations will be analysed from two different perspectives. Subsequently, the changes in the standard thermodynamic potentials and other variables will be calculated with two different corrections. In addition, the heat capacity which plays an important role in determining the stability for all cases will be investigated.

A. The First Law of Thermodynamics and Smarr's Formula

To evaluate the thermodynamic parameters of the Einstein-Euler-Heisenberg black hole, we will be using the Smarr's formula whose derivation can be carried out with the aid of Euler's homogeneous function theorem. With this purpose in mind, let us first express Euler's homogeneous function theorem [74]

$$f(x_1, x_2, \dots, x_n) = l^{-1} \left[i \frac{\partial f}{\partial x_1} x_1 + j \frac{\partial f}{\partial x_2} x_2 + \dots + k \frac{\partial f}{\partial x_n} x_n \right], \quad (10)$$

where λ is a constant, (i, j, \dots, k) are the integer powers and f represents a homogeneous function satisfying the homogeneity condition

$$f(\lambda^i x_1, \lambda^j x_2, \dots, \lambda^k x_n) = \lambda^l f(x_1, x_2, \dots, x_n). \quad (11)$$

Now, let us find the mass of metric (7). To establish the connection between Euler's homogeneous function theorem and Smarr's formula, one needs to set $r = r_h$ and equate the metric to function zero. As a result, the concerned mass function becomes

$$M(r_h, q, \mu) = \frac{r_h}{2} + \frac{q^2}{2r_h} - \frac{\mu q^4}{40r_h^5}. \quad (12)$$

Since for spherically symmetric black holes in four dimensions the Hawking-Bekenstein entropy in geometric units is

$$S = \pi r_h^2, \quad (13)$$

one can alternatively express black hole mass (12) as

$$M(S, q, \mu) = \frac{S^{1/2}}{2\pi^{1/2}} + \frac{q^2 \pi^{1/2}}{2S^{1/2}} - \frac{\mu q^4 \pi^{5/2}}{40S^{5/2}}. \quad (14)$$

If the variables in (14) are rewritten as

$$S \rightarrow \lambda^i S, \quad q \rightarrow \lambda^j q \quad \text{and} \quad \mu \rightarrow \lambda^k \mu \quad (15)$$

and the integer powers are set to satisfy

$$i = k = 2l \quad \text{and} \quad j = l, \quad (16)$$

Euler's homogeneous function theorem (10) enables one to write

$$M(S, q, \mu) = 2S \left(\frac{\partial M}{\partial S} \right) + q \left(\frac{\partial M}{\partial q} \right) + 2\mu \left(\frac{\partial M}{\partial \mu} \right). \quad (17)$$

This equation, referred to as the Smarr's formula, can alternatively be stated as

$$M = 2(ST_H + \mu \mathcal{A}) + q\Phi_e, \quad (18)$$

where Φ_e and \mathcal{A} represent the electric potential at the horizon and the conjugate quantity, respectively. By comparing Eqs.(10) and (17), the thermodynamic parameters of the Einstein-Euler-Heisenberg black hole can be determined. To start with, the Hawking temperature is evaluated as

$$T_H = \frac{\partial M}{\partial S} = \frac{1}{4\pi^{1/2}S^{1/2}} - \frac{q^2 \pi^{1/2}}{4S^{3/2}} + \frac{\mu q^4 \pi^{5/2}}{16S^{7/2}}, \quad (19)$$

whereas the electric potential at the horizon is found to be

$$\Phi_e = \frac{\partial M}{\partial q} = \frac{q}{r_h} \left(1 - \frac{\mu q^2}{10r_h^4} \right). \quad (20)$$

This result can be illustrated graphically for various q and μ values. Fig.(1) includes four graphs showing the mathematical trend of potential (20) for four randomly chosen electric charge values. The graphs suggest a correlation between the horizon value at which the electric potential reaches its peak and the Euler-Heisenberg parameter. The peaks are observed to reach higher values with increasing q and decreasing μ . For all cases, the effect of μ becomes irrelevant after the a certain horizon threshold, which also seems to be increasing with increasing q . Furthermore, a rise in μ is observed to cause a decrease in the peak value of the electric potential.

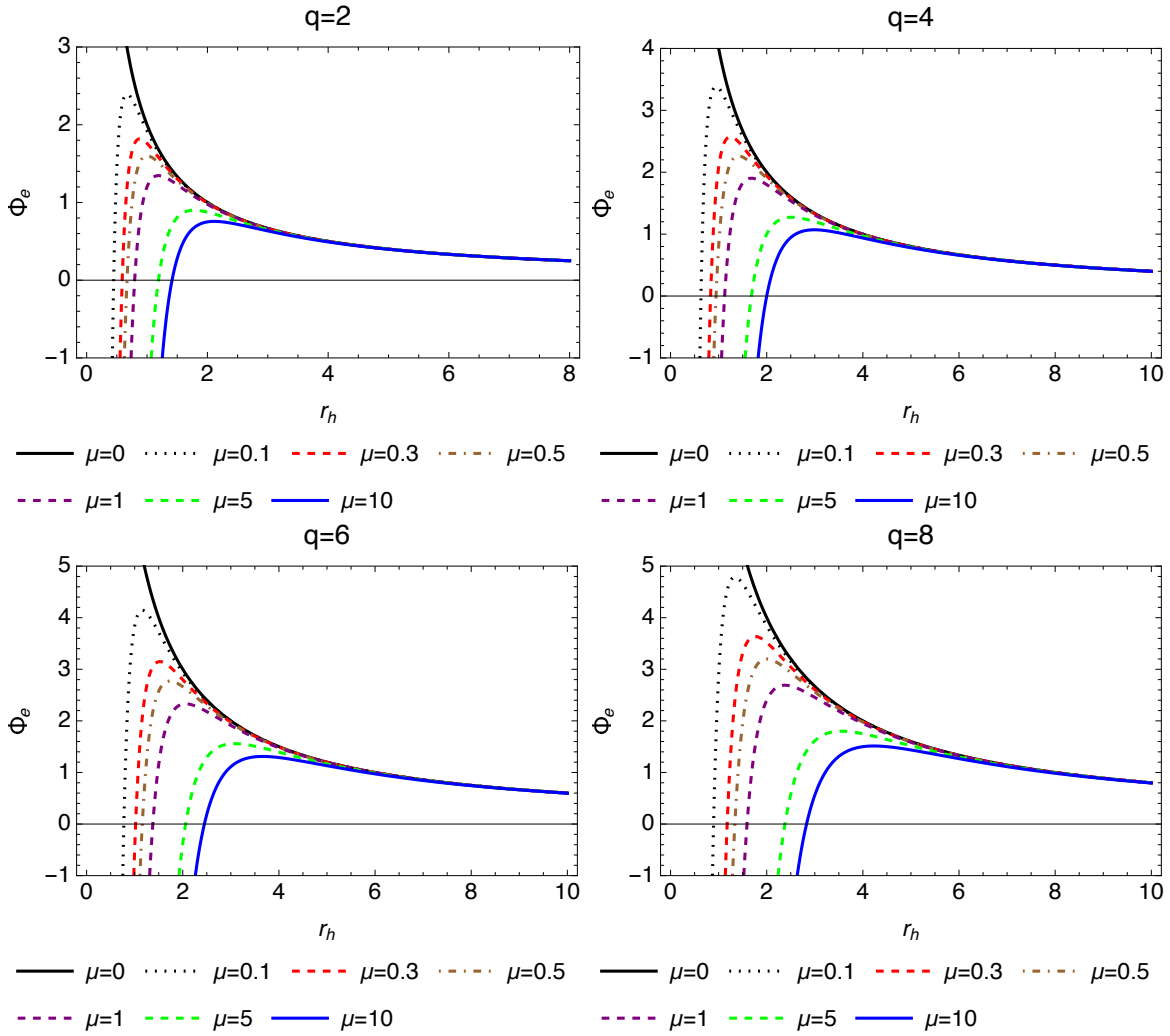


FIG. 1: The graphs show the relationship between the electric potential and the event horizon for different charge and EH parameter values.

The electric field of the Einstein-Euler-Heisenberg black hole becomes

$$\mathcal{E} = -\nabla\Phi_e\hat{r} = \frac{q}{r_h}\left(\frac{1}{r_h} - \frac{\mu q^2}{2r_h^5}\right)\hat{r}. \quad (21)$$

In Fig.(2), the behaviour of the electric field parallel to the electric potential is presented graphically for the different charge values chosen in the previous case. As expected, as the value of r_h increases, the peaks of the field are dampened. Additionally, an increase in the nonlinear parameter causes a shift of the peaks to higher r_h values, until they coincide at a certain horizon value. As before, this threshold value is observed to increase with increasing q .

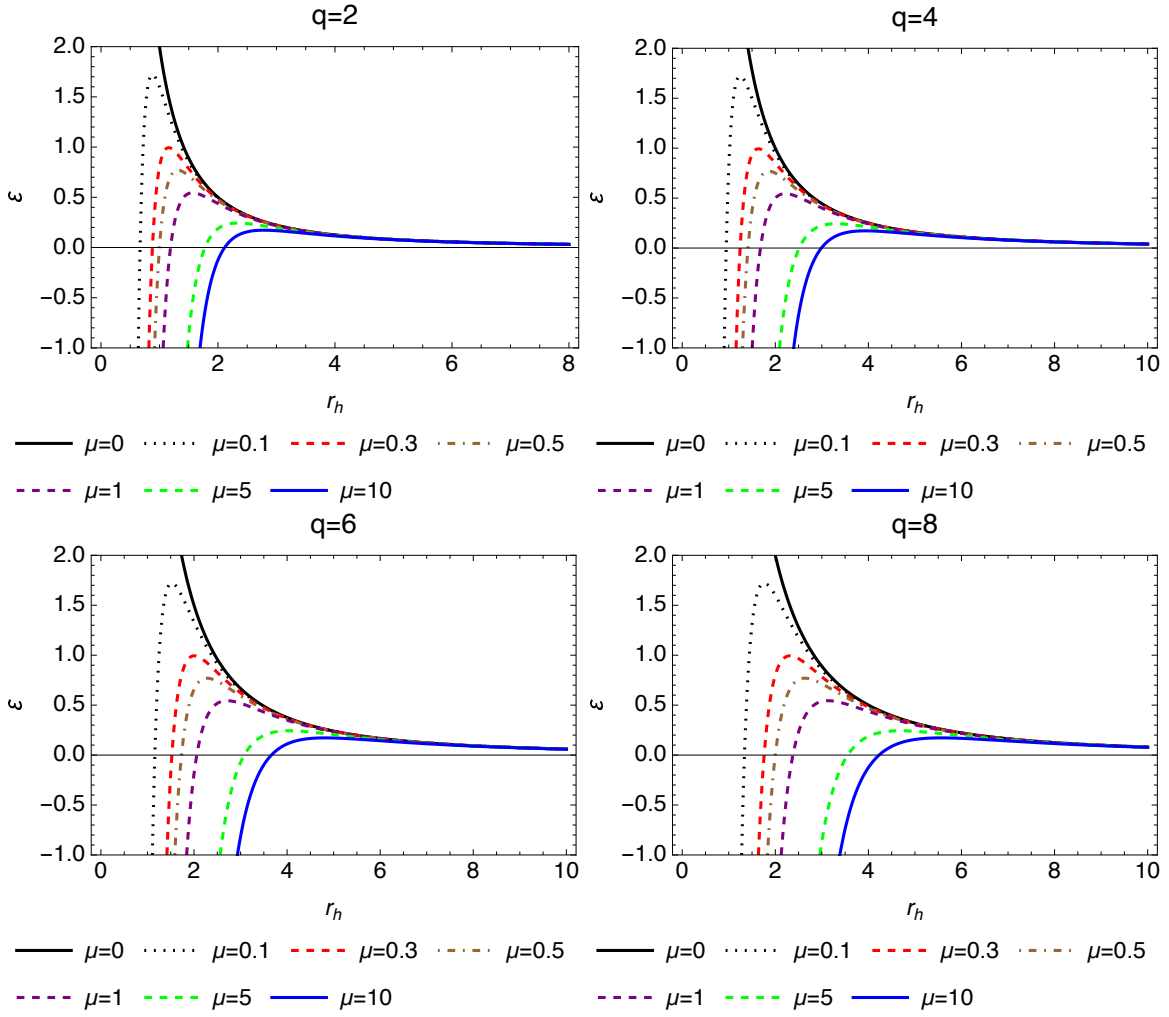


FIG. 2: The graphs illustrate behaviour the electric field for different charge and nonlinear parameter.

The conjugate quantity is evaluated as follows.

$$\mathcal{A} = \frac{\partial M}{\partial \mu} = -\frac{q^4 \pi^{5/2}}{40S^{1/2}}. \quad (22)$$

To express Hawking temperature in terms of horizon, one needs to substitute Eq. (13) into Eq. (19). Doing so results in

$$T_H = \frac{4r_h^6 - 4q^2 r_h^4 + \mu q^4}{16\pi r_h^7}, \quad (23)$$

which matches Eq.(8). This result can also be plotted for further analysis. In this context, Fig.(3) shows how the Hawking temperature behaves in relation to the horizon radius. From the graphs it is evident that when the event horizon radius decreases, the charge and the nonlinear parameter values increase, while the Hawking temperature increases. In the zero temperature case, the system has to be in the lowest energy state possible. Entropy is a function of the number of available microstates, and in many cases, there is only one state referred as the ground state with the lowest energy. Under such circumstances, the entropy at absolute zero will also be zero.

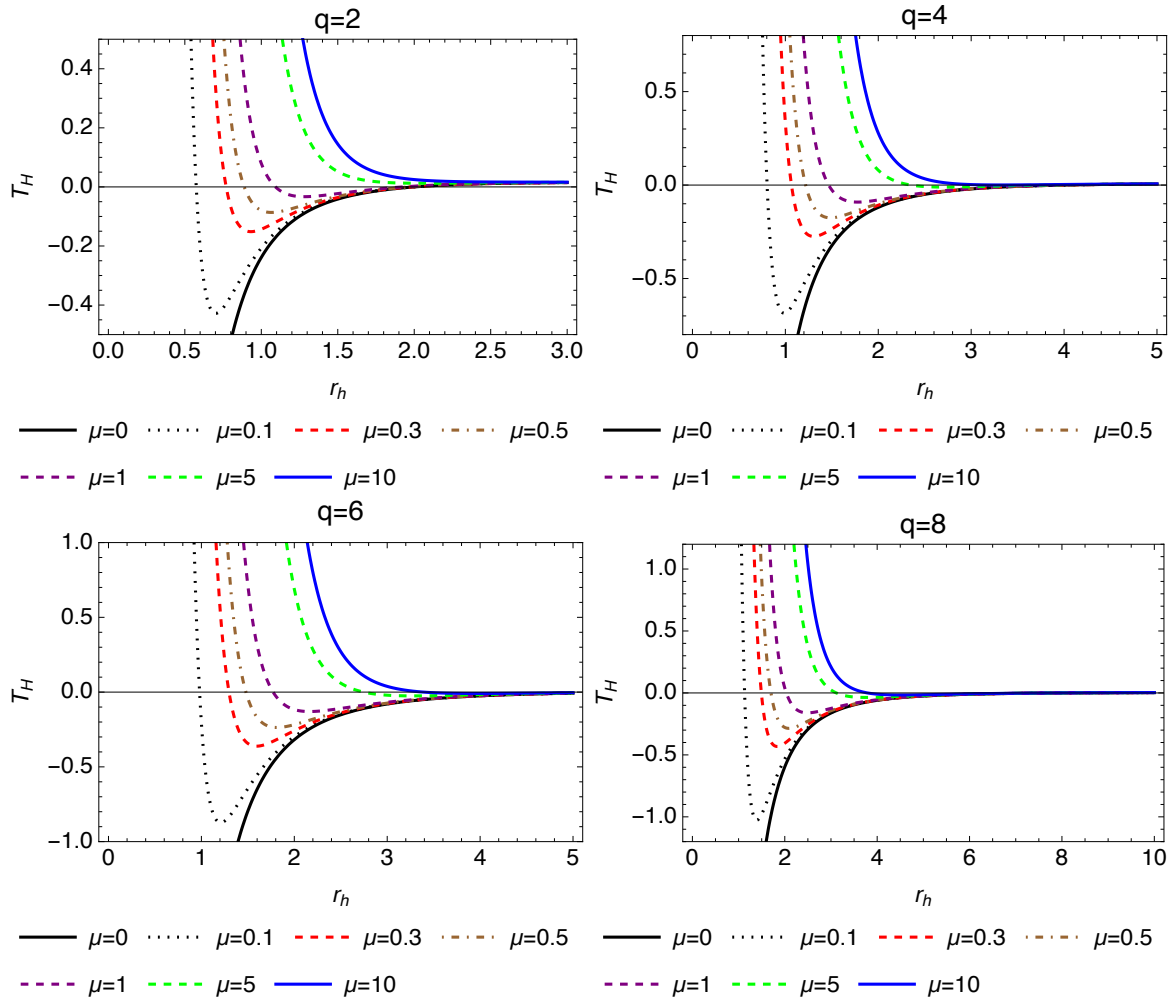


FIG. 3: Hawking temperature versus horizon radius for various q and μ values.

Having determined the Hawking temperature, one can now derive other thermodynamic quantities that also play a vital role in describing the state of the concerned black hole.

The black hole's Helmholtz free energy can be written as

$$F = - \int S dT_H = \frac{3q^2}{4r_h} + \frac{r_h}{4} - \frac{7\mu q^4}{80r_h^5}. \quad (24)$$

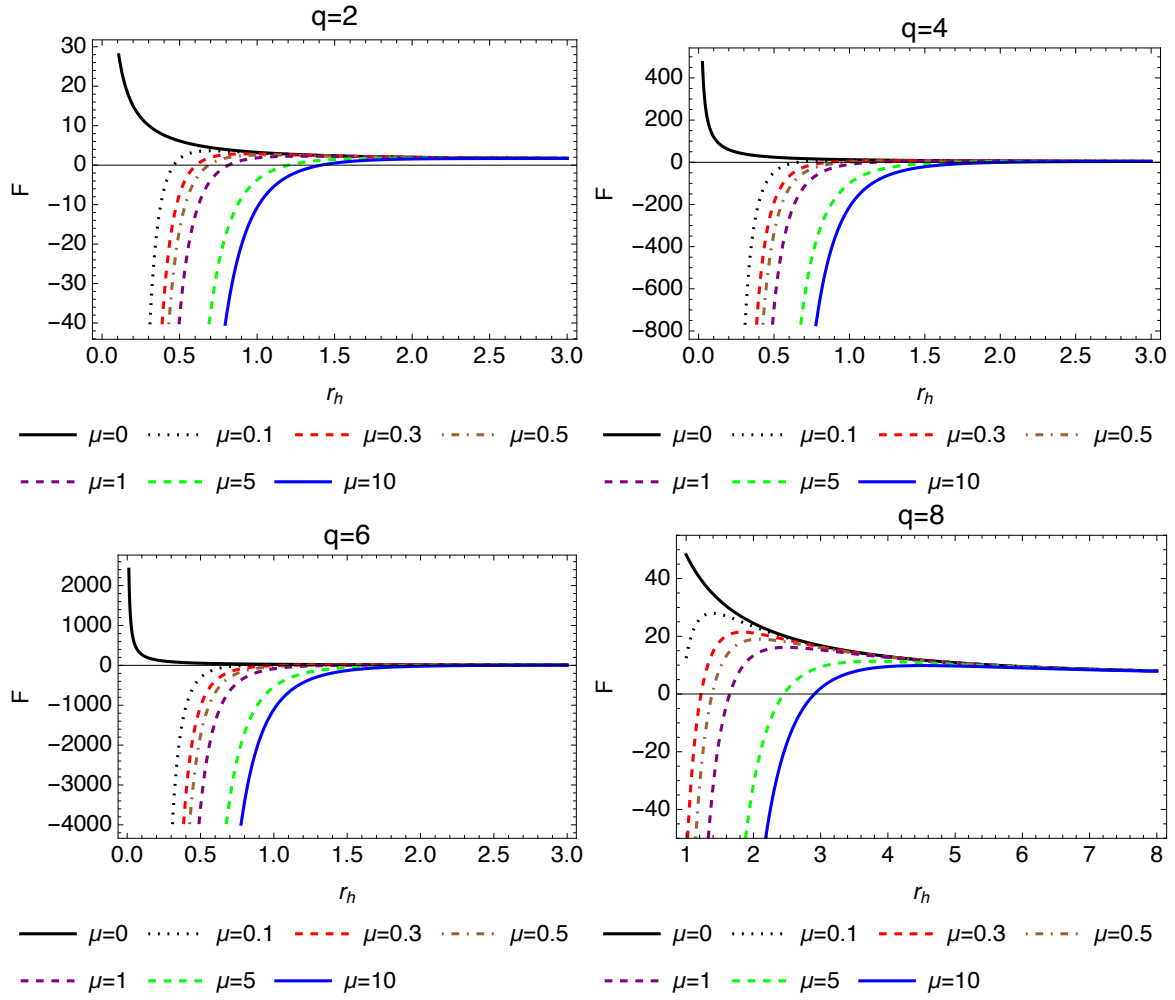


FIG. 4: The behaviour of Helmholtz free energy for different charge and NED parameter values. The effect of μ becomes negligible after a certain horizon value, which is observe to increase in accordance with electric charge parameter.

The internal energy, which determines the gravitational energy of the black hole and other thermodynamic interactions, is found as

$$E = \int T_H dS = \frac{r_h}{2} + \frac{q^2}{2r_h} - \frac{\mu q^4}{40r_h^5}. \quad (25)$$

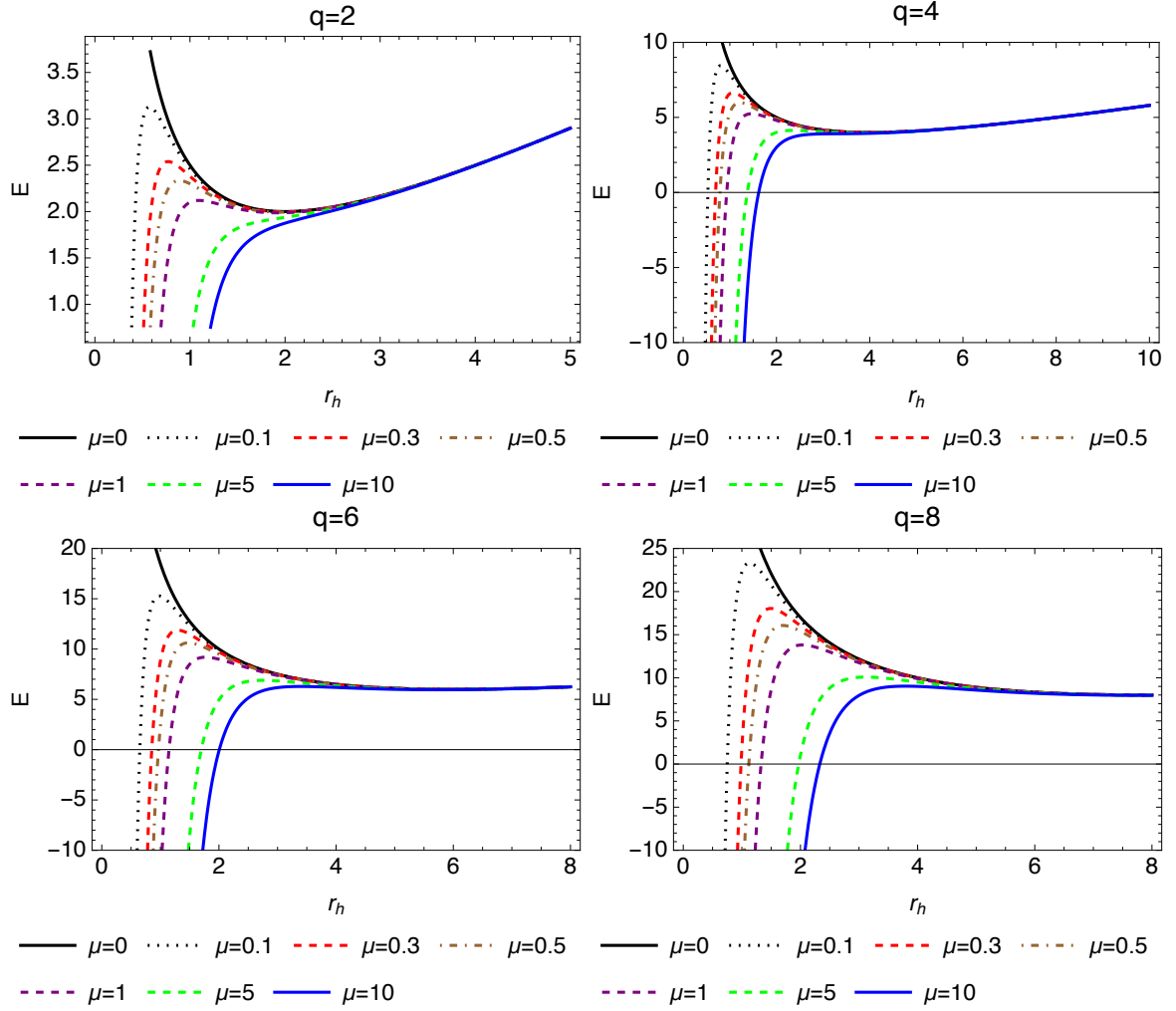


FIG. 5: The graphs above denote how internal energy of the concerned black hole behaves as a function of event horizon. The comparison of the plots show that the horizon value at which the NED parameter possesses no effect on the internal energy shifts to the right as the charge parameter increases.

Expressing pressure in term of horizon and the relevant parameter will help us to define important thermodynamic potentials. Therefor, let us define pressure of our thermodynamic system as

$$P = -\frac{dF}{dV}, \quad (26)$$

where $V = \frac{4}{3}\pi r_h^3$. Substituting Eq.(24) into Eq.(26) , the pressure of the black hole becomes

$$P = -\frac{dF}{dV} = -\frac{dF}{dr_H} \frac{dr_H}{dV} = \frac{1}{16\pi r_h^2} - \frac{3q^2}{16\pi r_h^4} + \frac{7\mu q^4}{64r_h^8}. \quad (27)$$

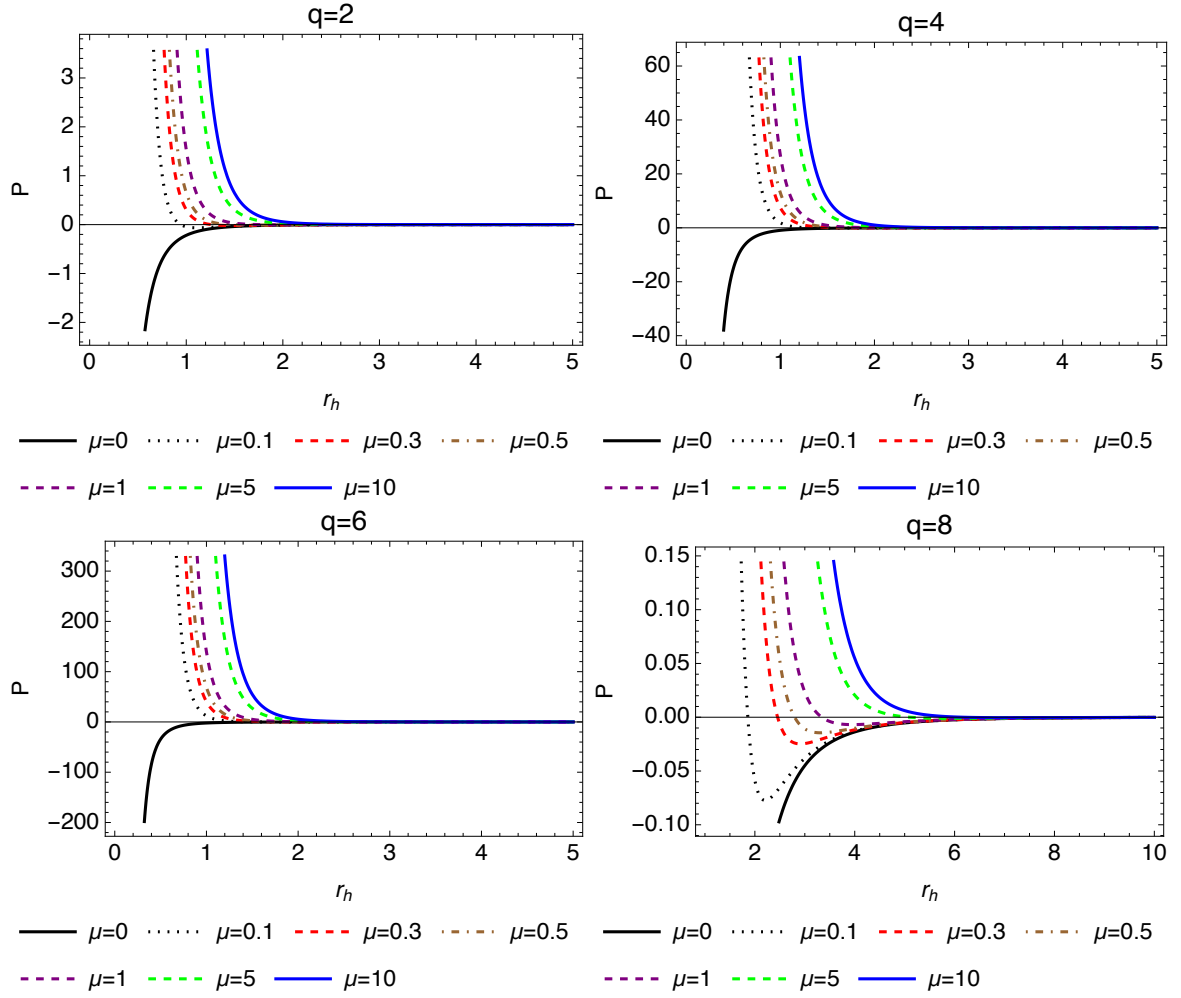


FIG. 6: Pressure versus black hole horizon for various q and μ values. For $q = 8$ the black hole seems to have a tendency towards undergoing an expansion for $\mu = 0.1, 0.3, 0.5$ and 1 . Furthermore, for all charge parameter values under consideration, the black hole exhibits no positive pressure when NED does not exist.

The enthalpy (H), which we can define by taking the combination of other thermodynamic variables, is given by

$$H = E + PV. \quad (28)$$

When we put the related variables into Eq.(28), Eq.(28) reduces to

$$H = \frac{5r_h}{12} - \frac{q^2}{4r_h} + \frac{29\mu q^4}{240r_h^5}. \quad (29)$$

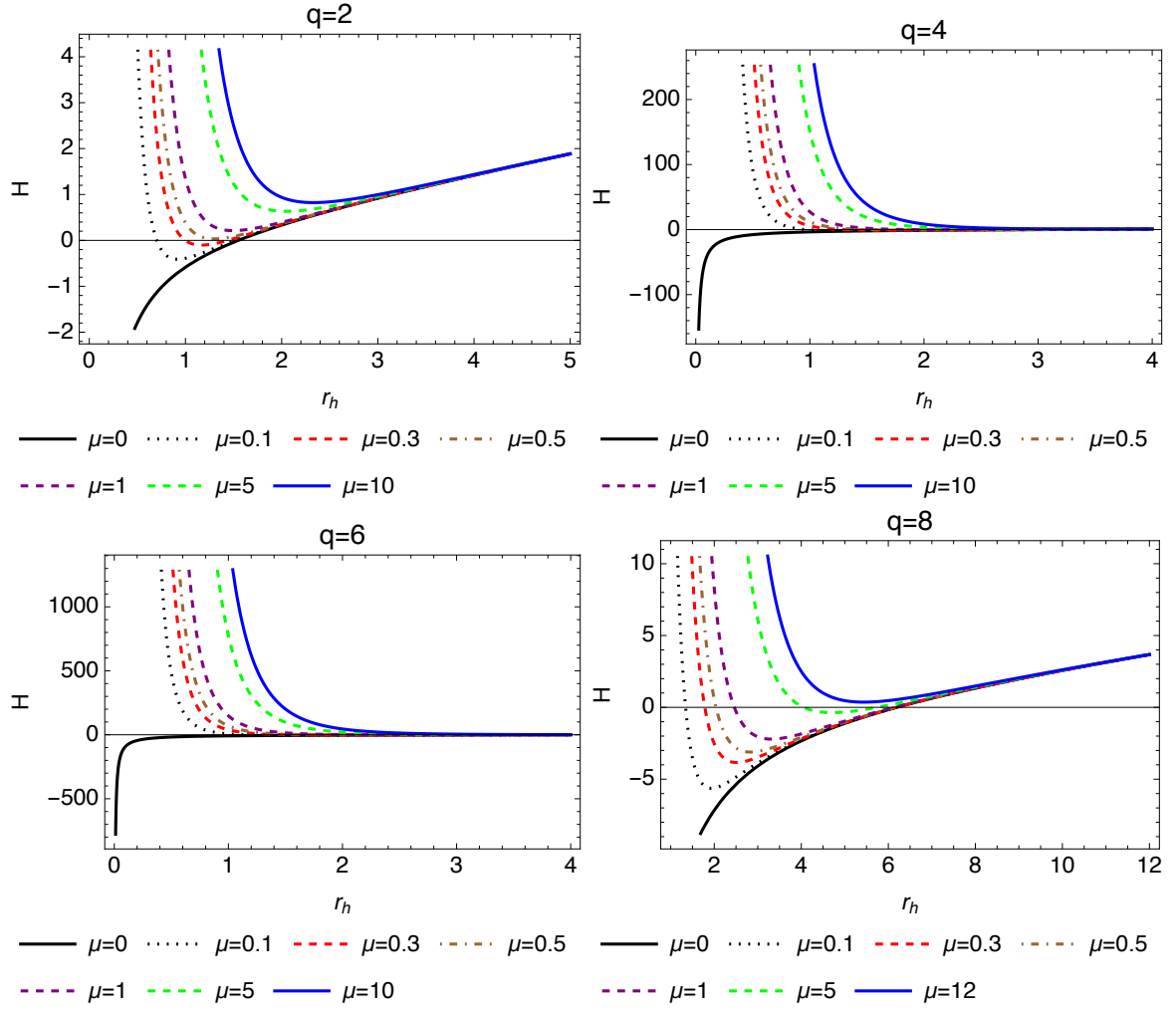


FIG. 7: In the graphs above, the effect of the nonlinear parameter on the enthalpy of the black hole is demonstrated for $q = 2, 4, 6$ and 8 . The behaviour of H for black holes whose charge parameter reads $q = 2$ resembles those with $q = 8$, while $q = 4$ and $q = 6$ are observed to behave in a similar manner.

Finally, the thermodynamic definition of Gibbs free energy is given by

$$G = F + PV. \quad (30)$$

Upon substitution of variables, obtain Gibbs free energy is obtained as

$$G = \frac{q^2}{2r_h} + \frac{r_h}{3} - \frac{7\mu q^4}{80r_h^5} + \frac{7\mu q^4}{48r_h}. \quad (31)$$

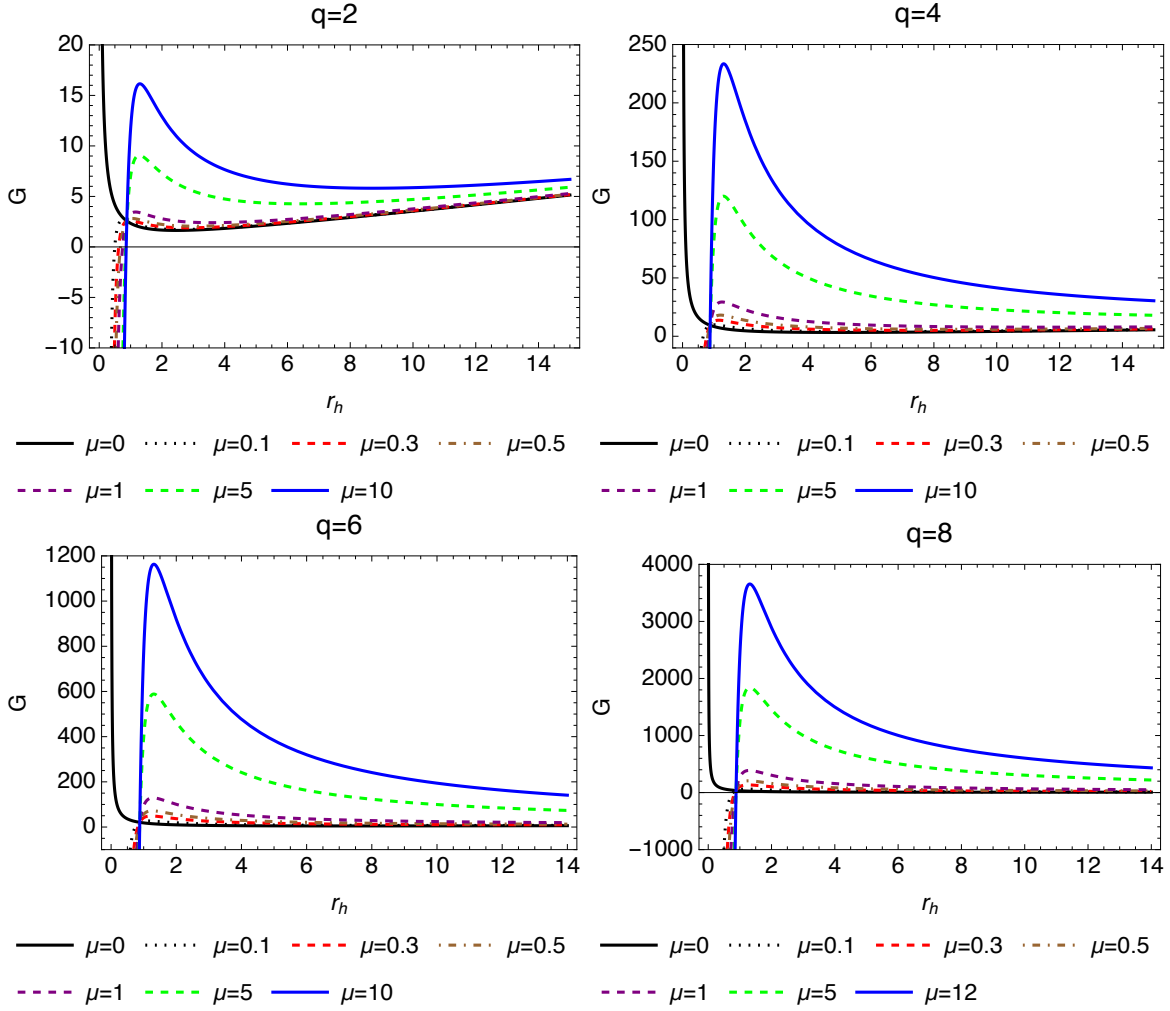


FIG. 8: The Gibbs free energy of an Einstein-Euler-Heisenberg black hole as a function of horizon for various q and μ values. The peaks exist only for the cases when the NED effects are present. The presence of such peaks within the Gibbs free energy of the black hole might be an indicator of a phase transition from a thermodynamic state to another.

Overall, the influence of the Euler-Heisenberg parameter on the thermodynamic quantities get more distinguishable as the charge of the black hole increases.

Having determined the majority of thermodynamic parameters, one can now focus on deriving the heat capacity of the concerned black hole, which plays a significant role in examining the stability of the thermal system under consideration. In this regard, the heat capacity can be figured via

$$C = T_H \left(\frac{\partial S}{\partial T_H} \right). \quad (32)$$

Upon the substitution of Eq.(23) and Eq.(13) in Eq.(32), one obtains

$$C = -2\pi r_h^2 \left(\frac{4r_h^6 - 4q^2 r_h^4 + \mu q^4}{4r_h^6 - 12q^2 r_h^4 + 7\mu q^4} \right). \quad (33)$$

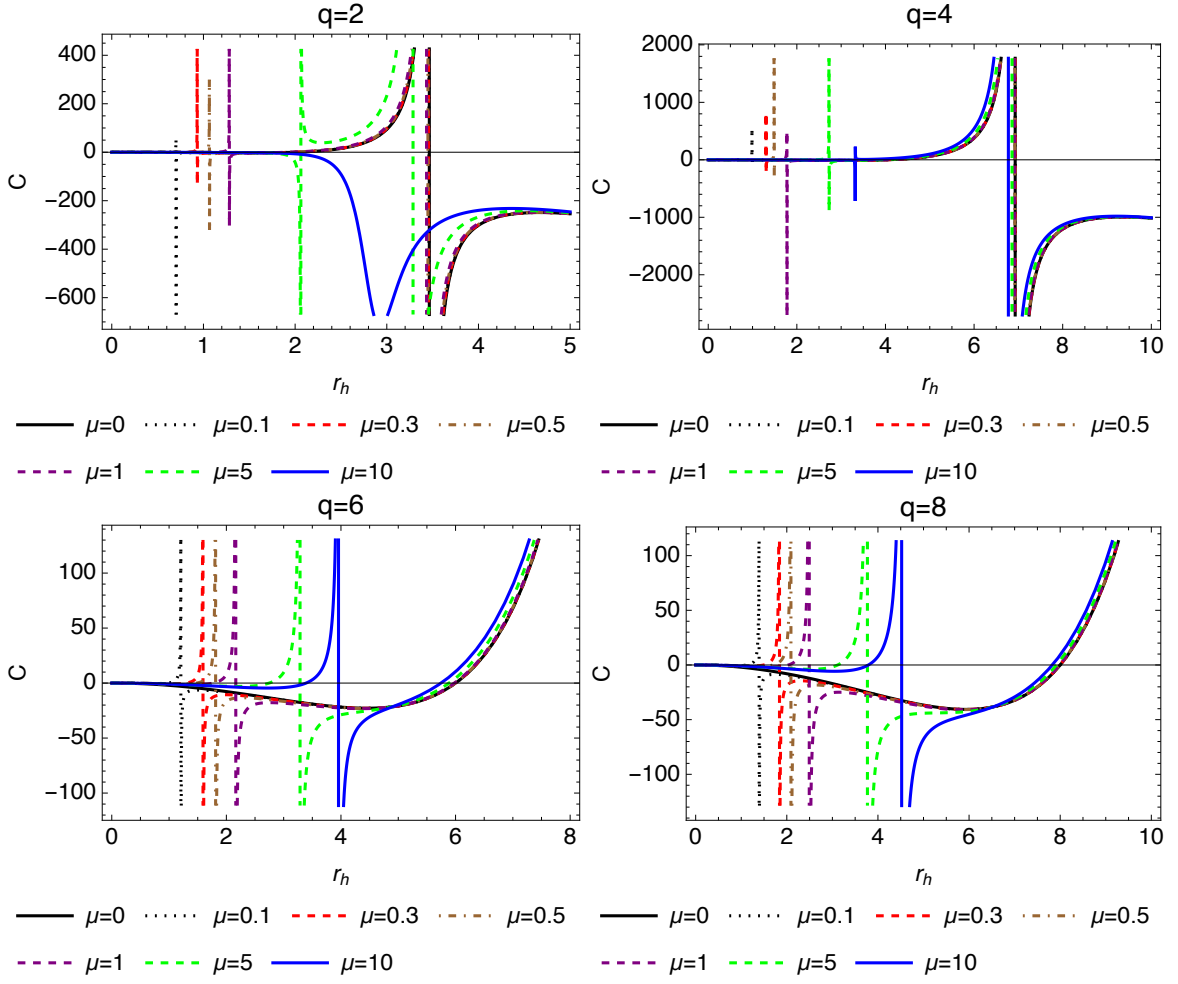


FIG. 9: The heat capacity versus event horizon graphs according to Eq.(33) for different charge and NED parameter values.

The plots presented in Fig.(9) show the behaviour of the heat capacity C as a function of r_h , under different choices of q and μ .

- $q = 2$: For small values of r_h , the black hole remains in an isothermal state across all nonlinear parameters for a short period. As r_h increases, however, the black hole experiences transitions to unstable states. Within these transitions, the nonlinear parameter is observed to play a critical role. Subsequently, for all Euler-Heisenberg parameters, the heat capacity is observed to converge in the negative domain.

With further analysis, an Einstein-Euler-Heisenberg black hole whose charge parameter reads $q = 2$ is found to experience phase shifts as long as $\mu \leq 9.142$ is satisfied. For $\mu = 9.143$, the black hole gets unstable and no phase transition takes place. To ensure $\mu = 9.142$ is the maximum limit of phase transitions (to four significant figures), the graph is replotted by setting $\mu = 10^{50}$ and no indication of stability or phase shift is identified for this extreme case either. For the relevant sketches, one can see Fig.(10).

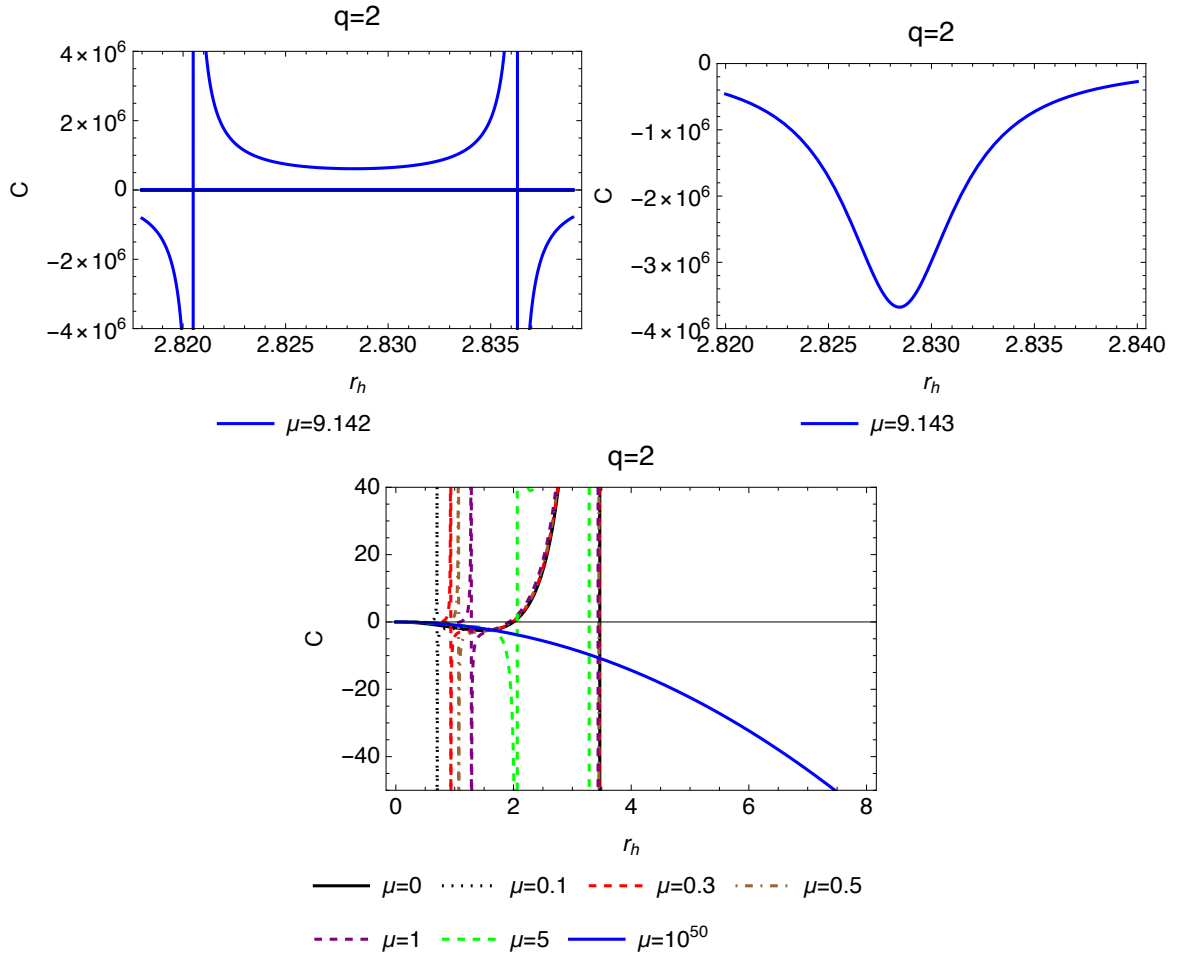


FIG. 10: The illustrations above respectively correspond to the behaviour of heat capacity for $\mu = 9.142$, $\mu = 9.143$ and $\mu = 10^{50}$. For all these cases, the charge parameter is kept constant at $q = 2$. Moreover, for $\mu = 9.143$ and $\mu = 10^{50}$, the behaviour of the heat capacity for lower values of the NED parameter are also included within the plots for the concerned horizon ranges.

- $q = 4$: Starting as an isothermal system for small values of r_h , the black hole undergoes phase transitions at different horizon values for different NED parameters. Phase transitions are observed to occur provided that $\mu \leq 36.57$, while $\mu = 36.57$ allows for two phase transitions which, according to the graphical analyses, are observed to take place within the range $5.645 < r_h < 5.666$ (see Fig.(11)). The black hole is unstable for $\mu = 36.58$ and beyond.

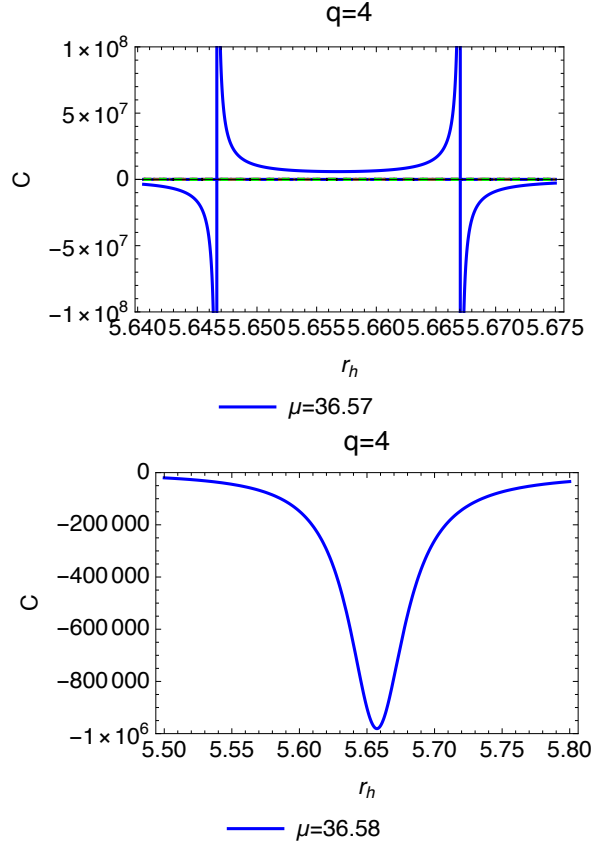


FIG. 11: These graphs represent how heat capacity behaves for $\mu = 36.57$ and $\mu = 36.58$. The last graph is plotted with the purpose of checking the stability of the system when the NED parameter reads $\mu = 36.58$. The charge parameter is $q = 4$ for all cases and smaller μ values are included within the plots, which are found to exhibit no special behaviour within the concerned horizon regimes.

- $q = 6$: The system remains in an isothermal state for a relatively longer period compared to other cases. As r_h increases beyond 1.5, the black hole undergoes sequential phase transitions. For horizon values beyond $r_h \geq 5$, heat capacity behaves in the same manner for all NED parameter values.

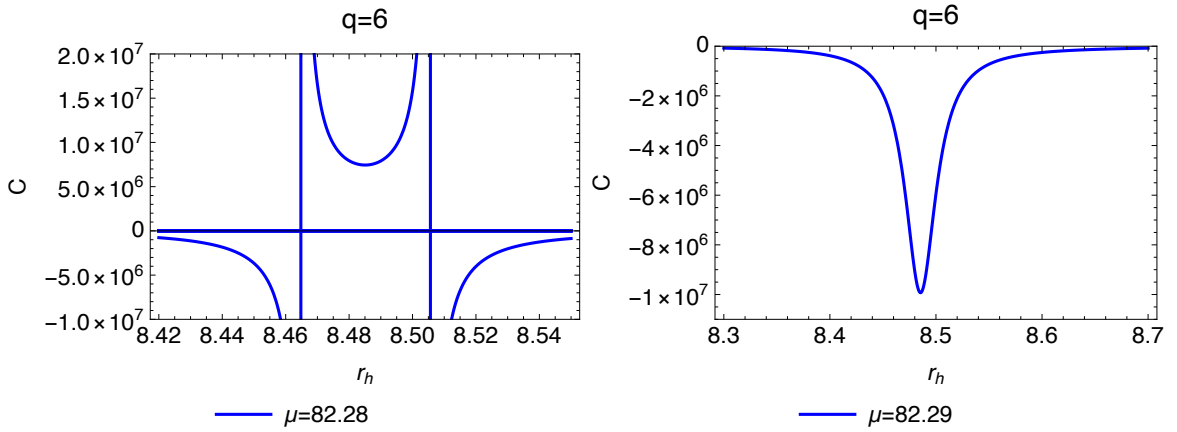


FIG. 12: In the plots above, one can see how heat capacity behaves for Einstein-Euler-Heisenberg black holes with $q = 6$ having $\mu = 82.28$ and $\mu = 82.29$, respectively. The detailed analysis has shown that for $\mu \leq 82.28$, phase shifts take place, whereas for higher NED parameters the heat capacity function varies smoothly.

- $q = 8$: Increasing q tends to enhance the extremity of divergences in C and shifts the critical points to higher

r_h values. Such a trend suggests significant roles for both q and μ in the dynamics and stability of the thermal system.

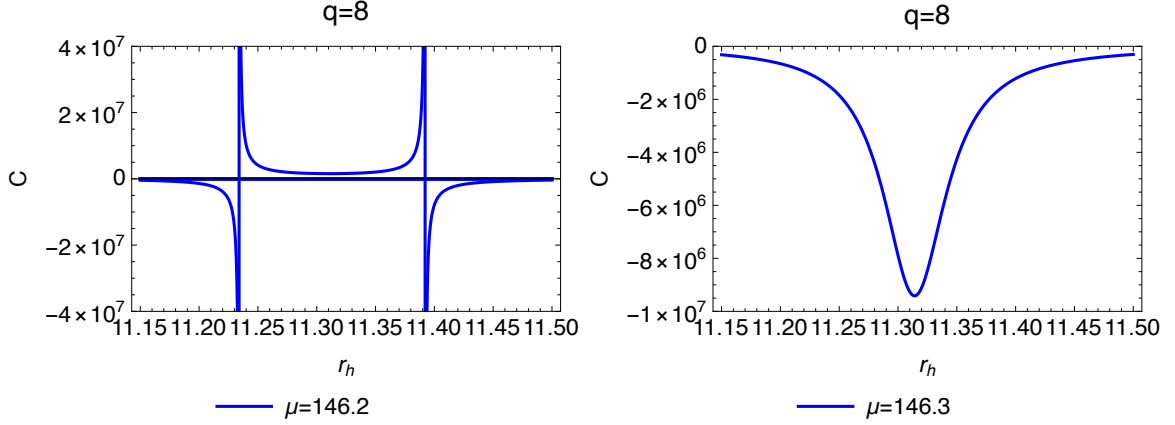


FIG. 13: The graphs above show that for an Einstein-Euler-Heisenberg black hole, phase transitions take place as long as $\mu \leq 146.2$, whereas for $\mu = 146.3$, the graph is smooth, showing no indications of phase transitions.

B. Corrections of Thermodynamic Parameters Based on Entropy

The thermodynamic variables under examination may undergo intriguing modifications if statistical mechanical corrections are added to the thermodynamic studies. In this framework, the fluctuations of the spacetime under study can be examined together with their impact on the macro scale properties of the system via statistical physics. With this purpose, let us use stability analysis to inspect the impact of logarithmic and exponential variations on the thermodynamics of Einstein-Euler-Heisenberg.

1. Logarithmic Corrections to Black Hole Entropy

Using the distribution function defined in [75], one may start investigating the logarithmic correction to the entropy based on definition of the partition function from the statistical mechanical perspective that goes as follows.

$$Z = \int_0^{\infty} \rho(\sigma) e^{-\beta\sigma} d\sigma, \quad (34)$$

in which $\beta = 1/T_H$ and σ represent the thermal average energy. To determine the density of states, which is the inverse Laplace transform of Eq.(34) for a certain energy, one can use

$$\rho = \frac{1}{2\pi i} \int_{c-i\infty}^{c+i\infty} e^{S(\beta)} d\beta, \quad (35)$$

where $S(\beta) = \beta\sigma + \ln Z$. To perform the above integral perturbatively using the saddle-point method, let us expand, at least in principle, the series expansion of entropy expression in the exponential term about the saddle-point β_0 can be written as

$$S(\beta) \approx S_0 + \frac{1}{2} (\beta - \beta_0)^2 \left(\frac{\partial^2 S}{\partial \beta^2} \right)_{\beta_0} + \dots, \quad (36)$$

in which S_0 is the zeroth order entropy. When Eq.(36) is substituted into Eq.(35), the density of states becomes

$$\rho = \frac{e^{S_0}}{2\pi i} \int_{c-i\infty}^{c+i\infty} e^{\frac{1}{2}(\beta-\beta_0)^2 \left(\frac{\partial^2 S}{\partial \beta^2} \right)_{\beta_0}} d\beta. \quad (37)$$

Consequently, the result of integral (37) comes out as [33]

$$\rho = \frac{e^{S_0}}{\sqrt{2\pi \left(\frac{\partial^2 \mathcal{S}}{\partial \beta^2} \right)_{\beta_0}}}. \quad (38)$$

Eventually, the microcanonical entropy at equilibrium can be written as

$$S_C = \ln \rho = S_0 - \frac{\alpha}{2} \ln S_0 T_H^2, \quad (39)$$

where α is the thermal fluctuation parameter [76]. In this work, the thermal fluctuation parameter will be taken as $\alpha = 1$ considering that the contribution from these fluctuations is at its highest when $\alpha = 1$. If Hawking temperature (23) and the zeroth order entropy πr_h^2 are plugged in Eq.(39), the microcanonical entropy of the system becomes

$$S_C = \pi r_h^2 - \frac{1}{2} \ln \left(\frac{(4r_h^6 - 4q^2 r_h^4 + \mu q^4)^2}{256 \pi r_h^{12}} \right). \quad (40)$$

The corrections on the internal energy of the system can be calculated using the general formula defined as

$$E_C = \int T_H dS_C. \quad (41)$$

substituting corrected entropy (40) and Hawking temperature (23) in Eq.(41), one finds

$$E_C = \frac{420\pi q^2 r_h^6 + 420\pi r_h^8 - 21\mu\pi q^4 r_h^2 + 140q^2 r_h^4 - 45\mu q^4}{840\pi r_h^7}. \quad (42)$$

Fig.(14) illustrates the behaviour of the logarithmically corrected internal energy as a function of r_h , under different charge and nonlinear parameters. Each curve represents the variation of E_C with r_h whose overall evaluation shows an increase in the charge parameter leads to a rise in the peak value of the logarithmically corrected internal energy, while an increase in the nonlinear parameter causes a decrease in the concerned peaks. As the value of r_h increases, the effect of the NED parameter becomes irrelevant and all functions coincide regardless of the charge parameter.

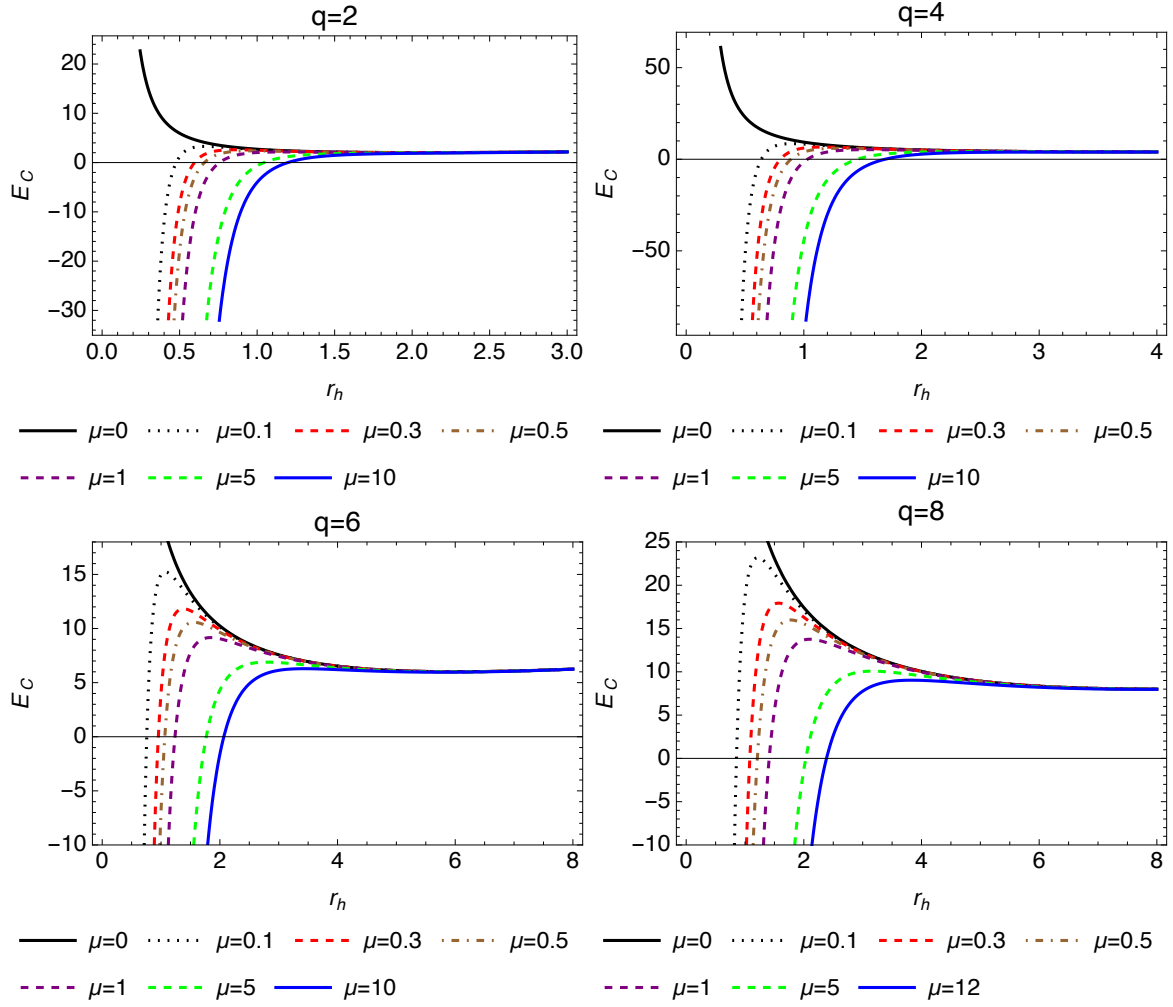


FIG. 14: Logarithmically corrected internal energy versus black hole horizon for various q and μ values. For $q = 2$ and $q = 4$, the corrections cause the turning points to disappear. However, for larger charge values the turning points remain unaffected

The Helmholtz free energy can be modified using the logarithmically corrected entropy as follows.

$$F_C = - \int S_C dT_H. \quad (43)$$

Plugging Eq.(40) and Eq.(23) into Eq.(43), one finds

$$\begin{aligned}
 F_C = & -\frac{1}{3360\pi r_h^7} \left[3\mu q^4 (98\pi r_h^2 + 60 + 35 \ln(256\pi)) \right. \\
 & - 105 (\mu q^4 - 4q^2 r_h^4 + 4r_h^6) \ln \left(\frac{(\mu q^4 - 4q^2 r_h^4 + 4r_h^6)^2}{r_h^{12}} \right) \\
 & - 140q^2 r_h^4 (18\pi r_h^2 + 4 + 3 \ln(256\pi)) \\
 & \left. + 420r_h^6 (-2\pi r_h^2 + \ln(256) + \ln(\pi)) \right]. \quad (44)
 \end{aligned}$$

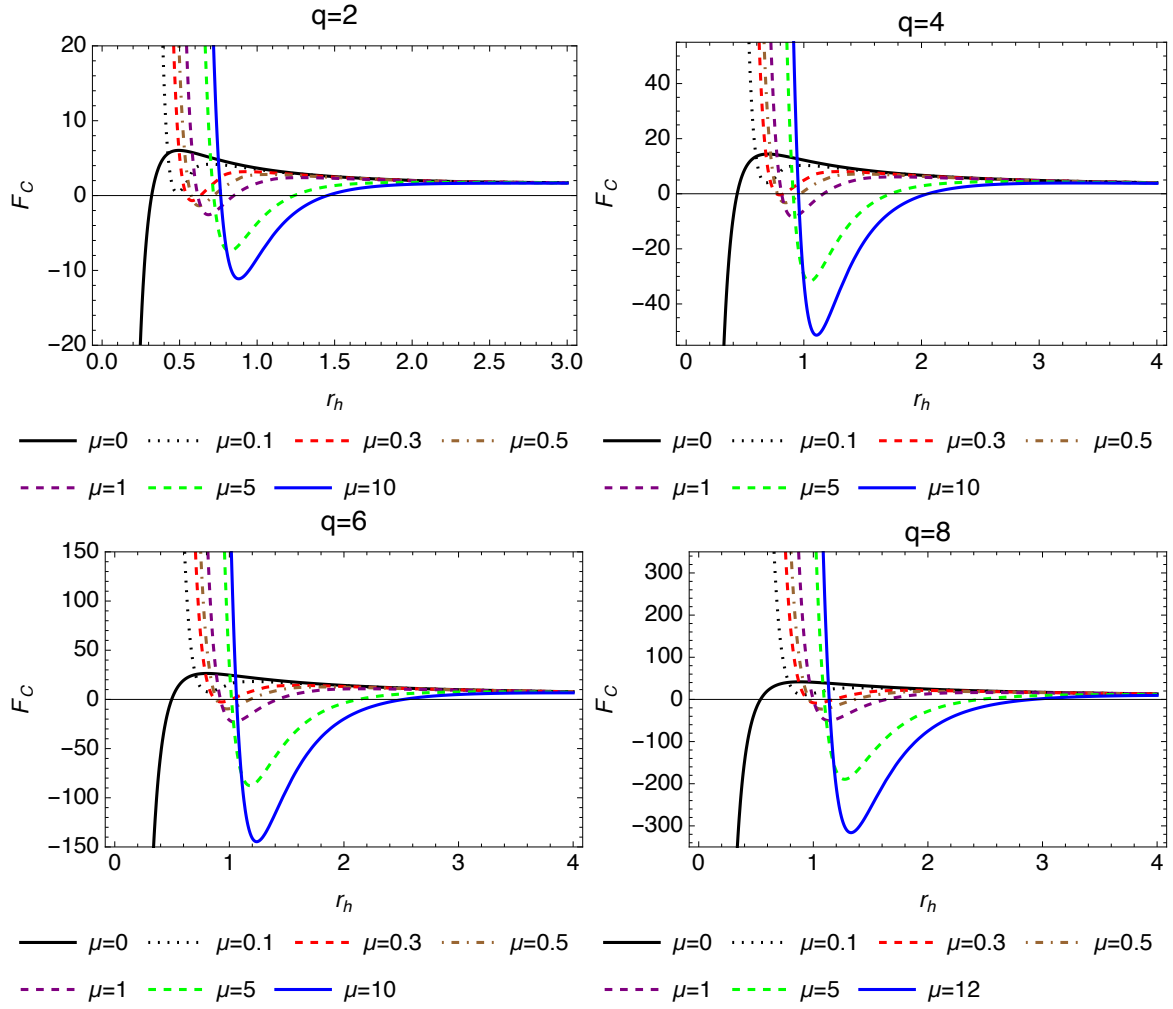


FIG. 15: Logarithmically corrected Helmholtz free energy versus black hole horizon for various q and μ values. Once these graphs are compared with the uncorrected ones, (see Fig.4) one notices that the trends are the exact opposite.

In Fig.(15), as in the logarithmically corrected internal energy, the influence of different μ values become apparent at small r_h values. Increasing the charge causes the values of the minimum values of corrected free energy to decrease. Also, increasing the nonlinear parameter values results in a shift of the minimum points towards higher negative values. When the r_h value increases, the contribution of the nonlinear parameter disappears.

After finding the logarithmically corrected Helmholtz free energy, the logarithmically corrected pressure can be calculated via

$$P_C = -\frac{dF_C}{dV}, \quad (45)$$

which results in

$$P_C = \frac{1}{128r_h^{10}\pi^2} \left[(12q^2r_h^4 - 4r_h^6 - 7\mu q^4) \ln \left(\frac{(-4q^2r_h^4 + 4r_h^6 + \mu q^4)^2}{r_h^{12}} \right) \right. \\ + (-12q^2r_h^4 + 4r_h^6 + 28\mu) \ln(\pi) \\ + (-96q^2r_h^4 + 32r_h^6 + 224\mu) \ln(2) \\ \left. + 8r_h^8\pi - 24q^2r_h^6\pi + 56\mu\pi r_h^2 + (-12q^4 + 48)\mu \right]. \quad (46)$$

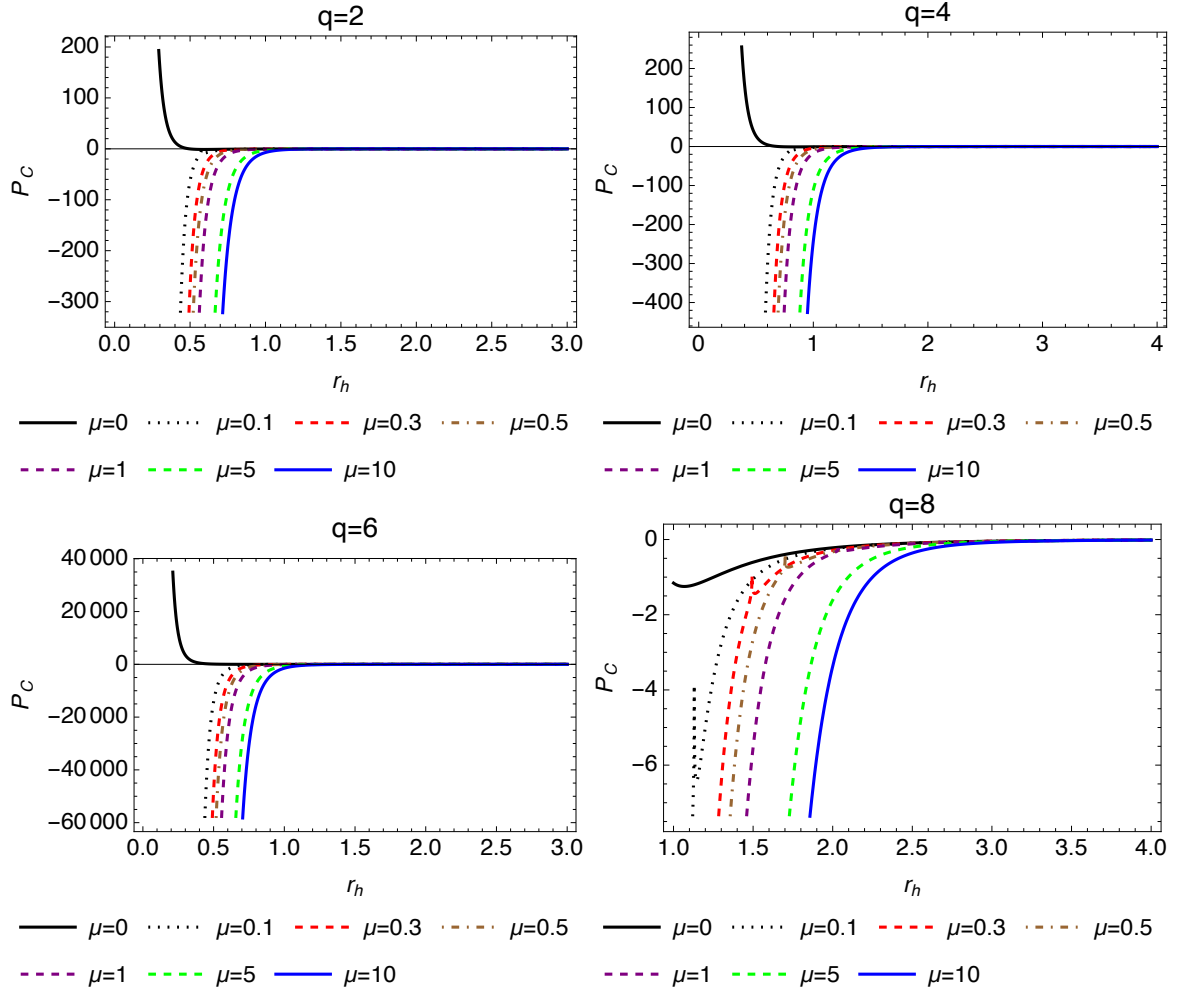


FIG. 16: Logarithmically corrected pressure versus the black hole horizon. The negative pressure values might give indications of a repulsive effect arising due to vacuum polarisation. Once all the pressure values coincide at zero, the black hole reaches an equilibrium state.

As can be seen in Fig.(16), increasing the charge and NED parameter values result in a black hole with negative pressure. This might suggest a resistance towards a possible collapse of the black hole.

Using the logarithmically corrected pressure and internal energy, Eq.(28) becomes

$$\begin{aligned}
 H_C = \frac{1}{3360\pi r_h^7} & \left[(420q^2 r_h^4 - 140r_h^6 - 245\mu q^4) \ln \left(\frac{(-4q^2 r_h^4 + 4r_h^6 + \mu q^4)^2}{r_h^{12}} \right) \right. \\
 & + (-420q^2 r_h^4 + 140r_h^6 + 980\mu) \ln(\pi) \\
 & + (-3360q^2 r_h^4 + 1120r_h^6 + 7840\mu) \ln(2) \\
 & + 1960\pi r_h^8 + 840\pi q^2 r_h^6 \\
 & + 560q^2 r_h^4 - 84 \left(q^4 - \frac{70}{3} \right) \pi \mu r_h^2 \\
 & \left. - 180\mu \left(-\frac{28}{3} + \frac{10}{3} q^4 \right) \right], \tag{47}
 \end{aligned}$$

which represents the logarithmically corrected enthalpy.

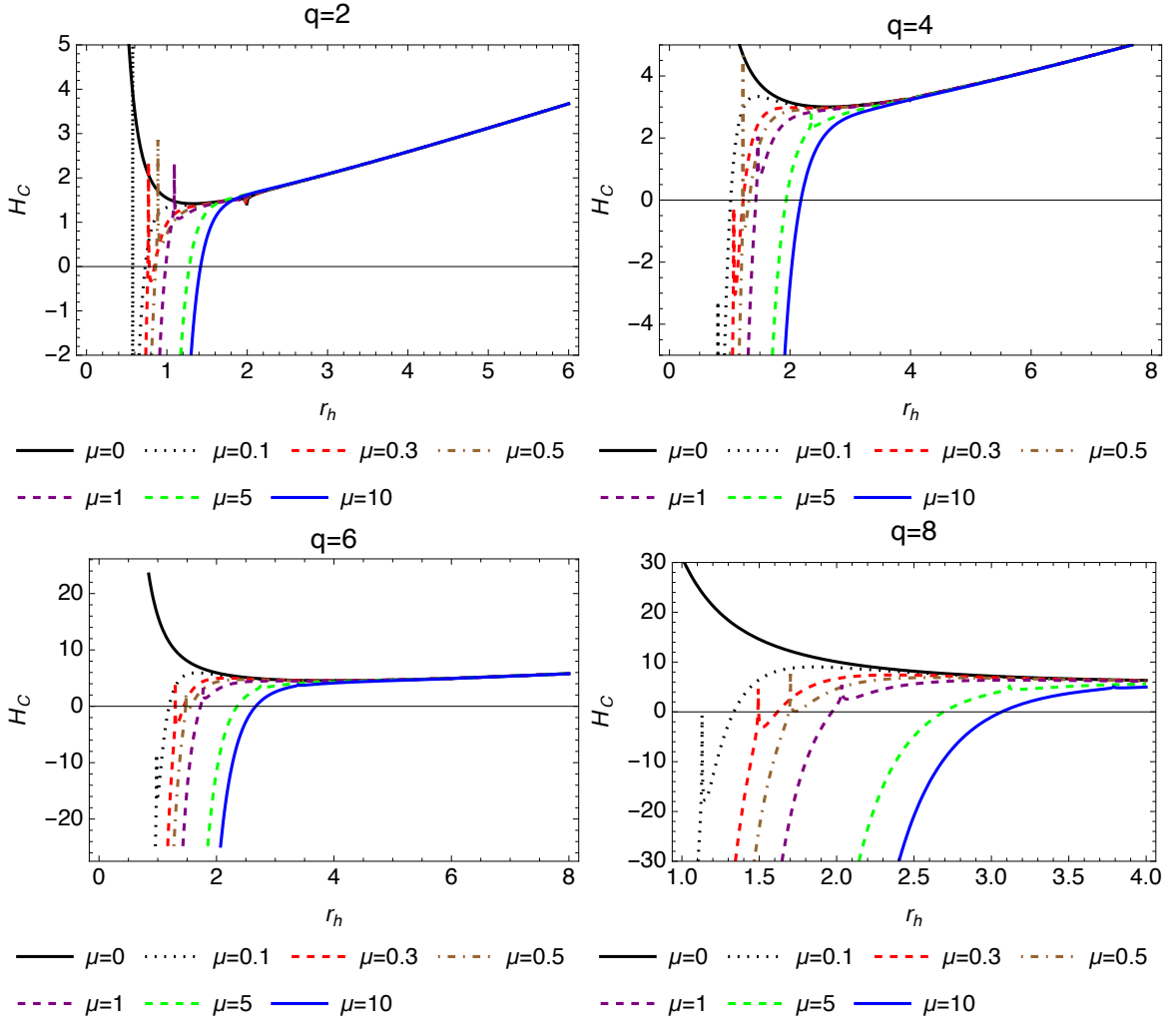


FIG. 17: Logarithmically corrected enthalpy versus black hole horizon. For all charge parameter values the corrected enthalpy roughly behaves as reflections of its uncorrected versions through the x-axis.

The behaviour of the logarithmically corrected enthalpy in relation to the event horizon radius is shown in Fig.(17). The graphics show that the gradient of the corrected enthalpy declines behaviour with increasing radius, eventually reaching to the same values for all NED parameters.

Also, the logarithmically corrected Gibbs free energy is determined as

$$\begin{aligned}
 G_C = \frac{1}{840\pi r_h^7} & \left[420\pi q^2 r_h^6 + 280\pi r_h^8 + 70 \ln \left(\frac{(-4q^2 r_h^4 + 4r_h^6 + \mu q^4)^2}{r_h^{12}} \right) r_h^6 \right. \\
 & - 70 \ln(\pi) r_h^6 - 560 \ln(2) r_h^6 - 35 \ln \left(\frac{(-4q^2 r_h^4 + 4r_h^6 + \mu q^4)^2}{r_h^{12}} \right) \mu q^4 \\
 & \left. + 140q^2 r_h^4 - 105\mu q^4 + 196\mu\pi r_h^2 + 140 \ln(\pi)\mu + 1120 \ln(2)\mu + 240\mu \right], \tag{48}
 \end{aligned}$$

following Eq.(30).

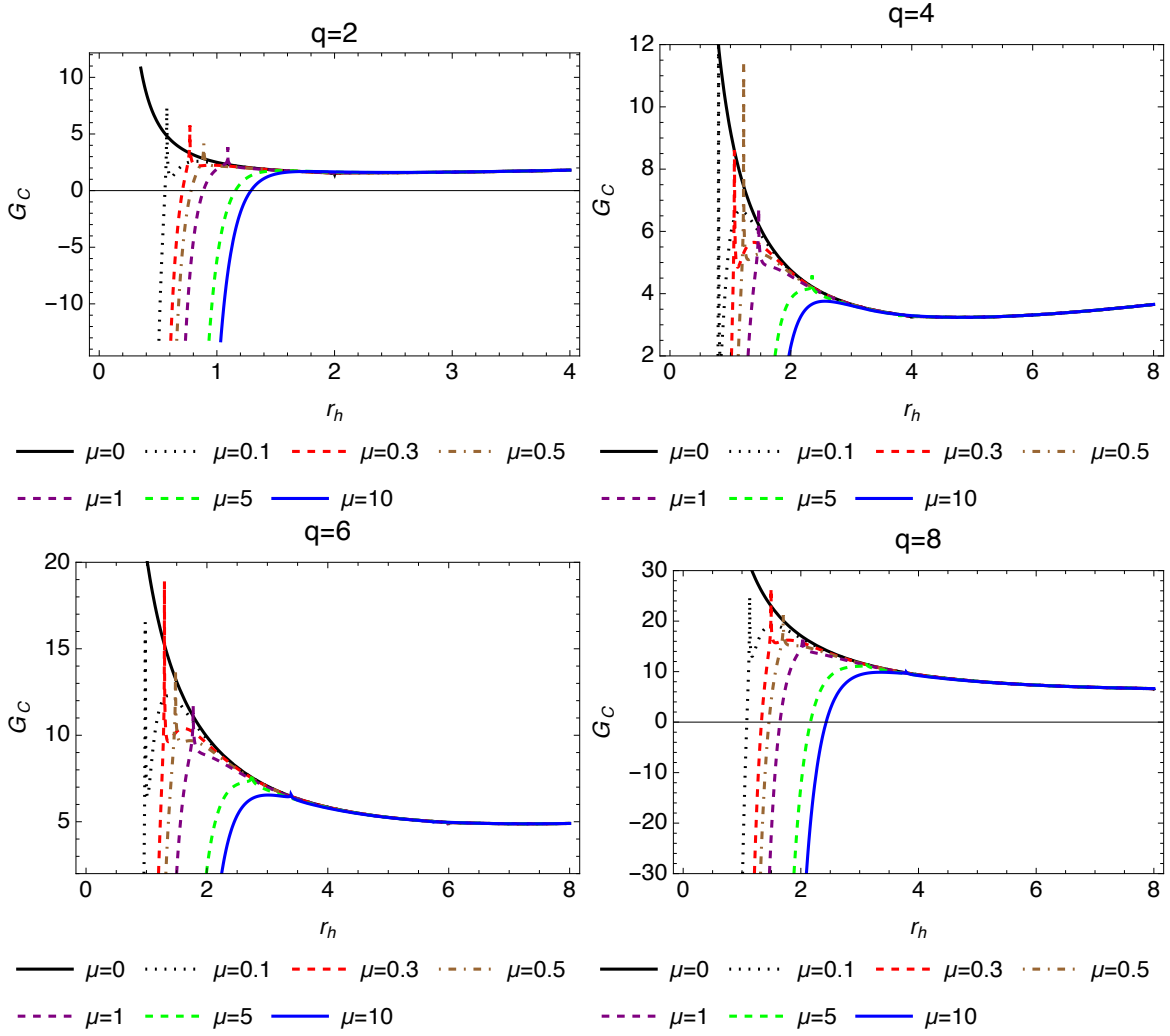


FIG. 18: Logarithmically corrected Gibbs free energy versus black hole horizon for various q and μ values.

The graphs in Fig.18 are displayed to investigate the behaviour of the logarithmically Gibbs free energy and the impact of thermal variations. When these graphs are compared with the ones given in Fig.8, one notices a drastic change in the behaviour of the peak points. To be more specific, the peaks observed in Fig.8 are sharp, while those in Fig.18 experience a smooth variations.

To define the logarithmically corrected heat, one must use

$$C_C = \frac{dE_C}{dT_H}. \quad (49)$$

In this context, the corrected logarithmically heat capacity can be written as

$$C_C = \frac{2\mu\pi q^4 r_h^2 + 6\mu q^4 - 8\pi q^2 r_h^6 + 8\pi r_h^8 - 8q^2 r_h^4}{-7\mu q^4 + 12q^2 r_h^4 - 4r_h^6}. \quad (50)$$

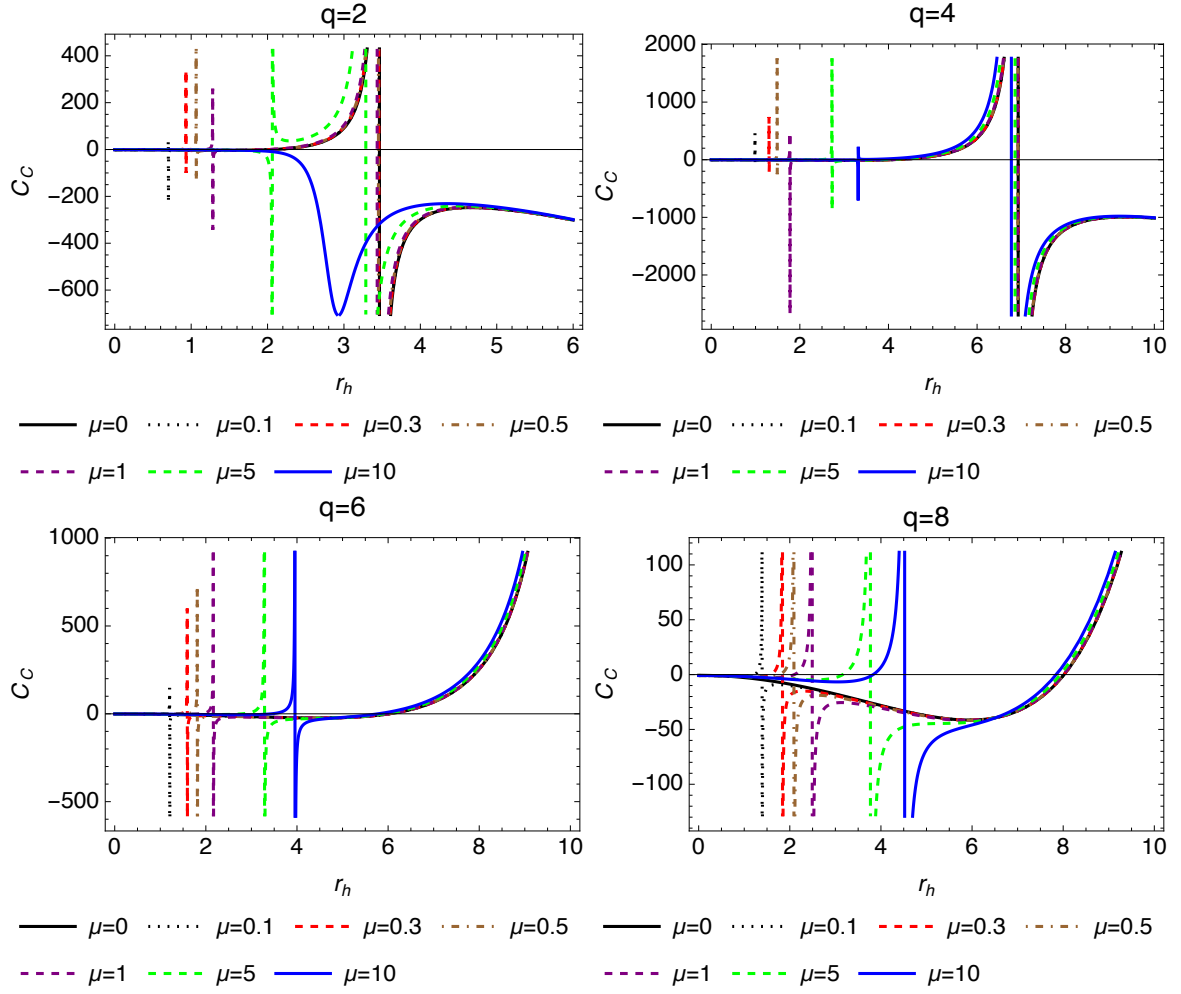


FIG. 19: Logarithmically corrected heat capacity versus the black hole horizon for various q and μ values.

- $q = 2$: Just like in the uncorrected case, the Einstein-Euler-Heisenberg black hole possesses an isothermal state for small horizon values and the heat capacity converges in the negative domain for $r_h > 4$. Fig.20 shows that for $q = 2$, the constraint on the NED parameter for the allowance of phase transitions remains as $\mu \leq 9.142$ to four significant figures, as in the uncorrected case.

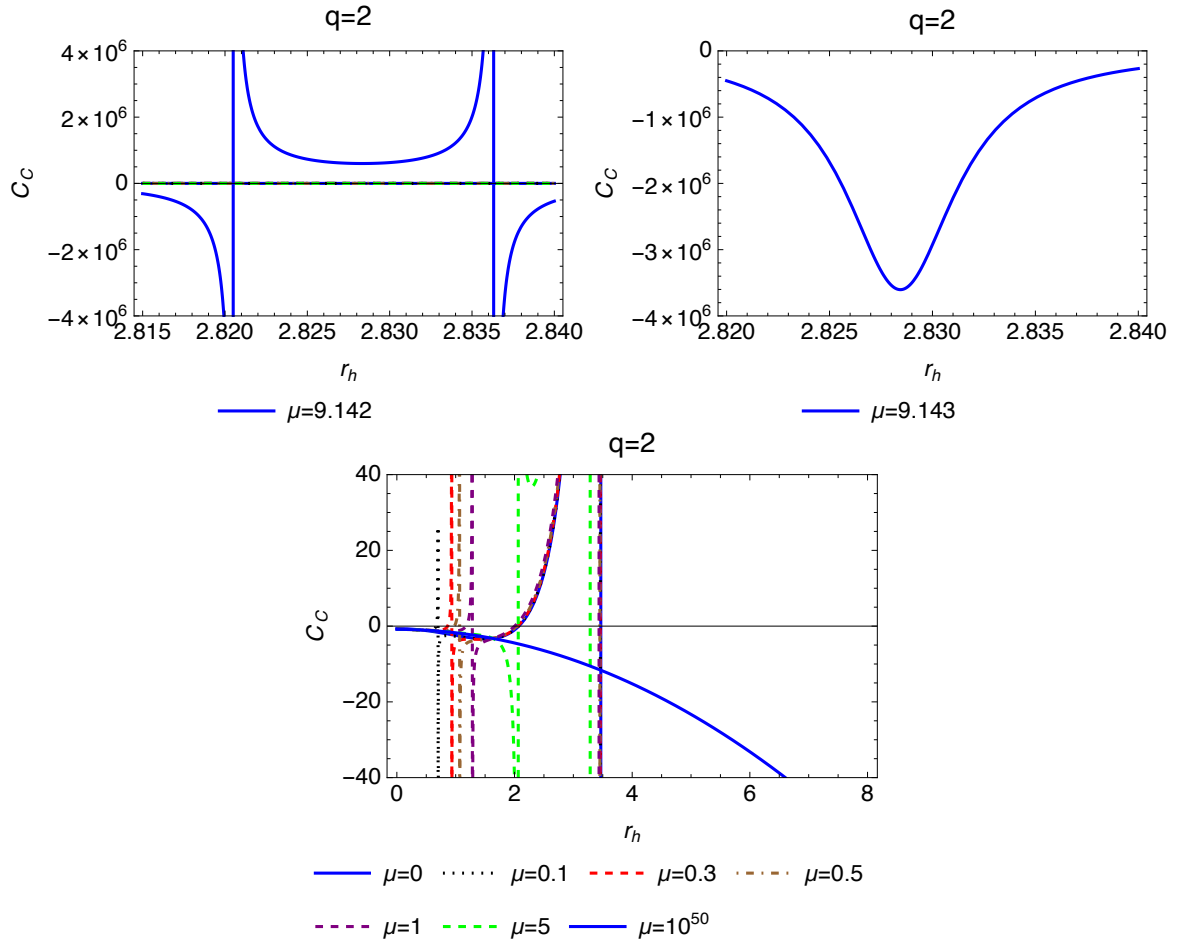


FIG. 20: The behaviour of heat capacity for $\mu = 9.142$, $\mu = 9.143$ and $\mu = 10^{50}$ for $q = 2$.

- $q = 4, 6$ and 8 : For all these cases, no significant changes are observed in the behaviour of the heat capacity. Furthermore, the upper limit of the NED parameter allowing phase transitions also remain unchanged regardless of the charge parameter. For further details, one can check Figures 21, 22 and 23.

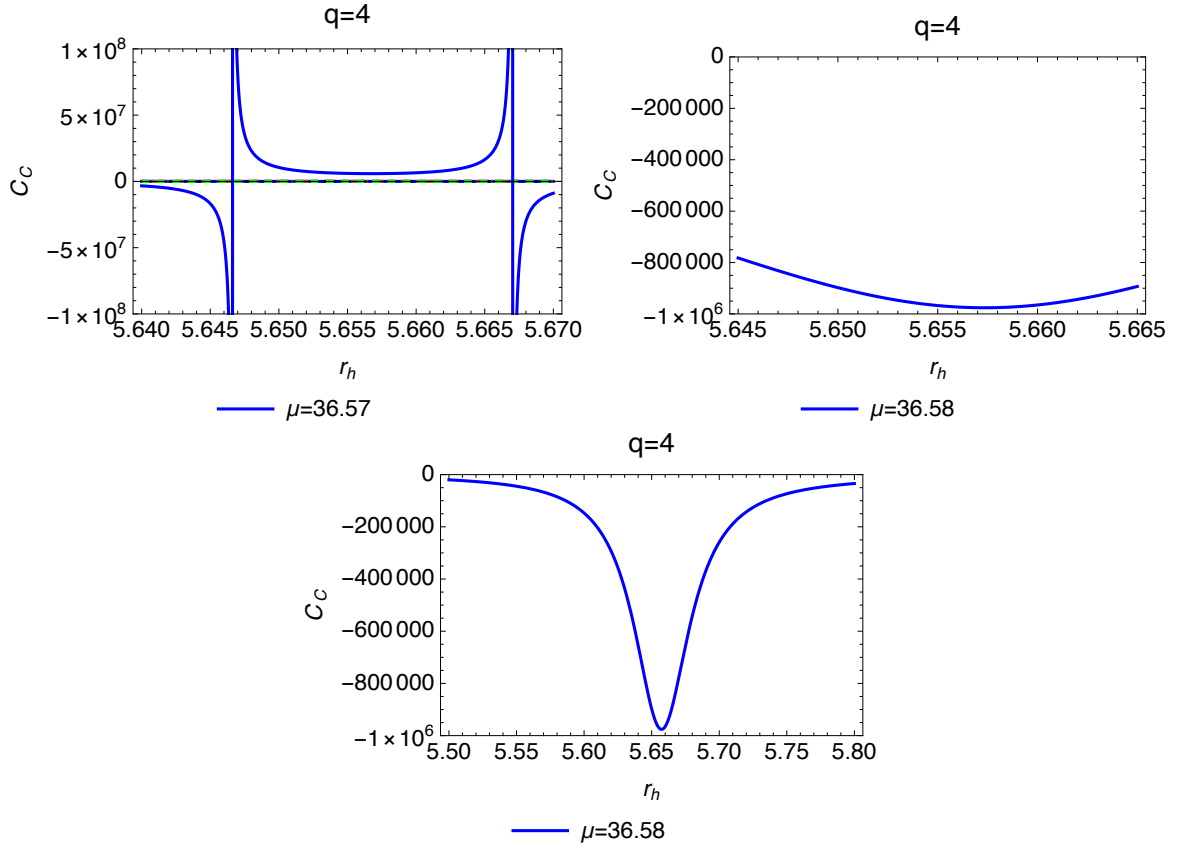


FIG. 21: The plots above show that for phase transitions to be possible, the NED parameter should not exceed 36.57 (to four significant figures). For $\mu \geq 36.58$, the black hole is unstable.

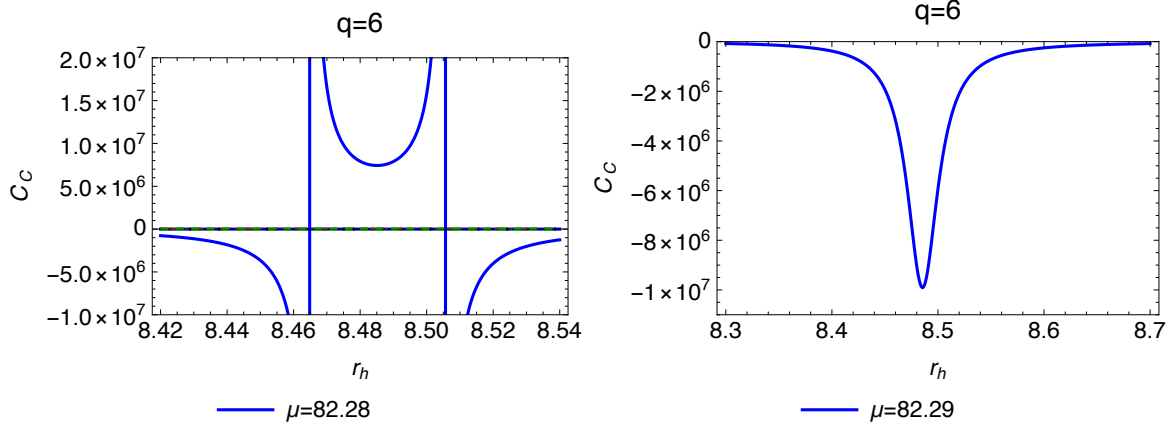


FIG. 22: the detailed examination of heat capacity versus horizon to determined the upper limit of the NED parameter for phase shifts to possible take place. No change has occurred in this upper limit compare to the uncorrected case.

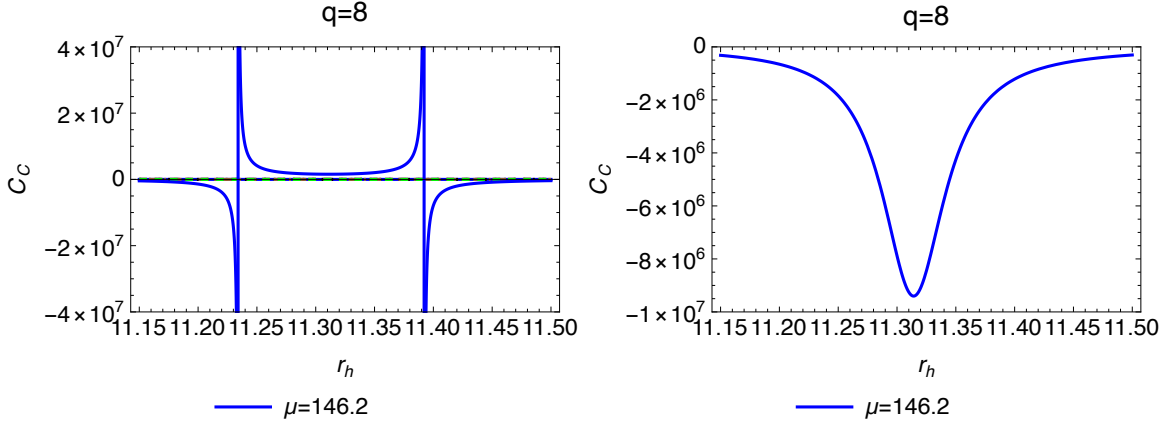


FIG. 23: For $\mu \leq 146.2$, there exist indications of phase transitions, like in the uncorrected case.

2. Exponential Corrections to Black Hole Entropy

The exponential correction to the black hole entropy in Euler-Heisenberg NED when can be discuss microstate counting is done for quantum states that are only present on the horizon. In this case, the entropy of the black hole receives an exponential correction [54]. The exponential statistical correction can be applied by treating the black hole as a system consisting of a set of N micro-particles. In this context, the number of different permutations of the elements in the statistical ensemble is given as [54]

$$\Omega = \frac{(\sum s_i)!}{\prod s_i!}, \quad (51)$$

in which s_i the is the repetition number of each particle. Also note that, when n_i and ϵ_i are the number of each particle and the energy of the i th microstate, respectively, the total number of micro-particles and the total energy of the statistical system can be written as

$$\begin{aligned} N &= \sum s_i n_i, \\ E &= \sum s_i n_i \epsilon_i. \end{aligned} \quad (52)$$

The variation of $\ln \Omega$ under the constraints $\delta \sum s_i n_i = 0$ and $\sum \epsilon_i \delta (s_i n_i) = 0$ gives the repetition number of the particles as

$$s_i = \left(\sum s_i \right) e^{-\lambda n_i}, \quad (53)$$

where λ is the variation parameter. Therefore, the constraint $\sum e^{-\lambda n_i} = 1$, the large N approximation and the entropy definition $S = \lambda N$ all together enable one to define the exponentially corrected entropy as [54]

$$S^{EC} = S_0 + e^{-S_0}. \quad (54)$$

Starting from the following definition the exponentially internal energy and substituting Hawking temperature (23) in Eq. (41), one gets

$$E^{EC} = \frac{1}{8} \left(\operatorname{erfi}(\sqrt{\pi} r_h) \left(\frac{4}{15} \pi^3 \mu q^4 - 4\pi q^2 + 2 \right) - \frac{\mu q^4 \left(e^{\pi r_h^2} (4\pi^2 r_h^4 + 2\pi r_h^2 + 3) + 3 \right)}{15 r_h^5} + \frac{4q^2 \left(e^{\pi r^2} + 1 \right)}{r_h} + 4r_h \right), \quad (55)$$

in which “erfi” represents the error function.

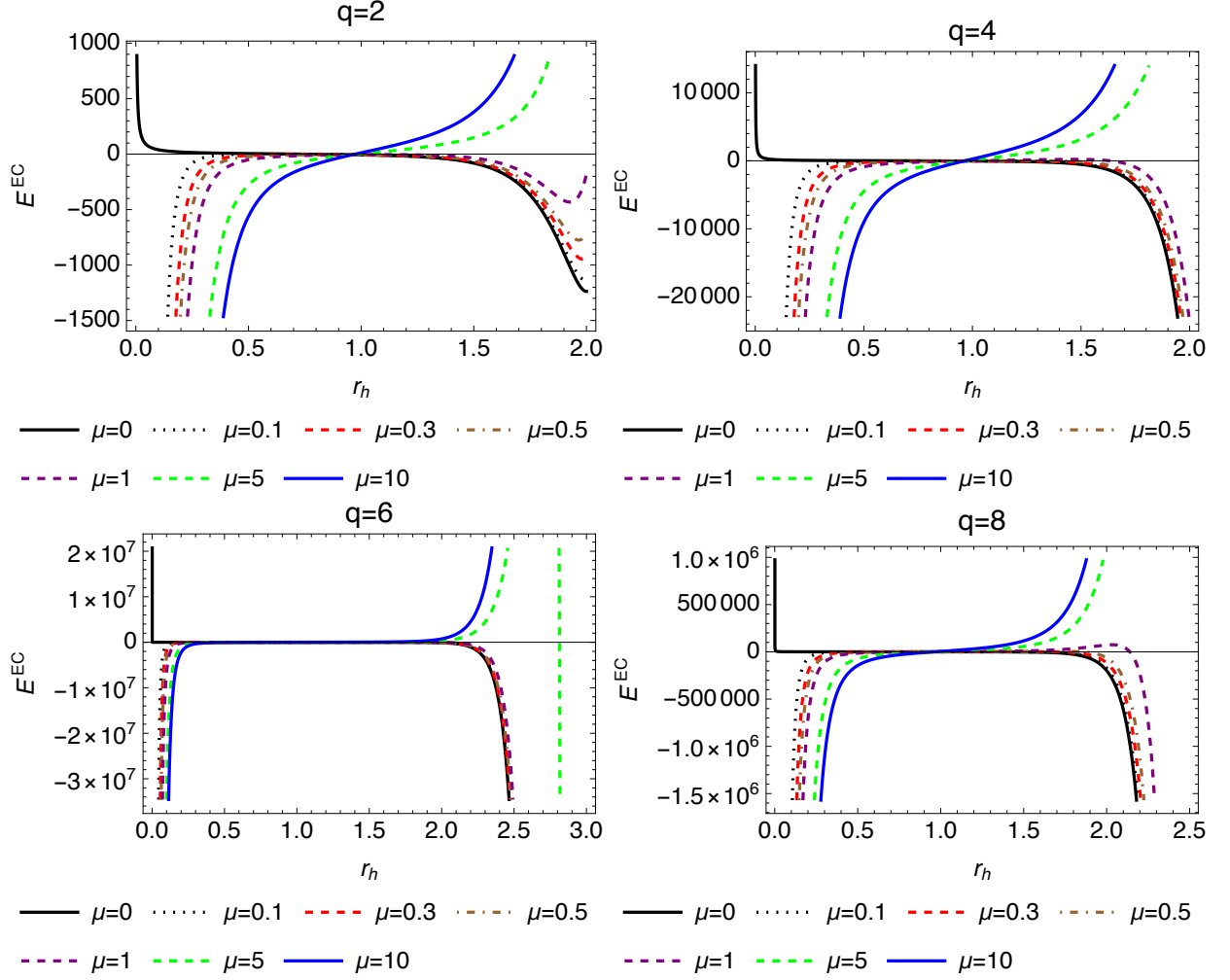


FIG. 24: Exponentially corrected internal energy versus black hole horizon for various q and μ values.

Fig.(24) shows the evolution of the exponentially corrected internal energy against r_h for different charge and nonlinear parameter values. The main difference between these graphs and the ones drawn for the uncorrected and the logarithmically corrected internal energies can be seen for $r_h > 1$ when the charge parameters are $q = 2, 4$ and 8 , whereas for $q = 6$ this threshold value shifts to $r_h > 2$. Regardless of the charge parameter values, all functions start divergent after the mentioned threshold horizon values towards a preferred direction depending on the NED value.

The exponentially corrected Helmholtz free energy becomes

$$\begin{aligned}
 F^{EC} = \frac{1}{240\pi r_h^7} & \left[4\pi r_h^7 \operatorname{erfi}(\sqrt{\pi} r_h) (2\pi^3 \mu q^4 - 30\pi q^2 + 15) \right. \\
 & + 3\pi r_h^2 (-7\mu q^4 + 60q^2 r_h^4 + 20r_h^6) \\
 & \left. + e^{\pi r^2} (60r_h^4 ((2\pi q^2 - 1)r_h^2 + q^2) - \mu q^4 (8\pi^3 r_h^6 + 4\pi^2 r_h^4 + 6\pi r_h^2 + 15)) \right], \tag{56}
 \end{aligned}$$

following the same procedure as the exponentially corrected internal energy.

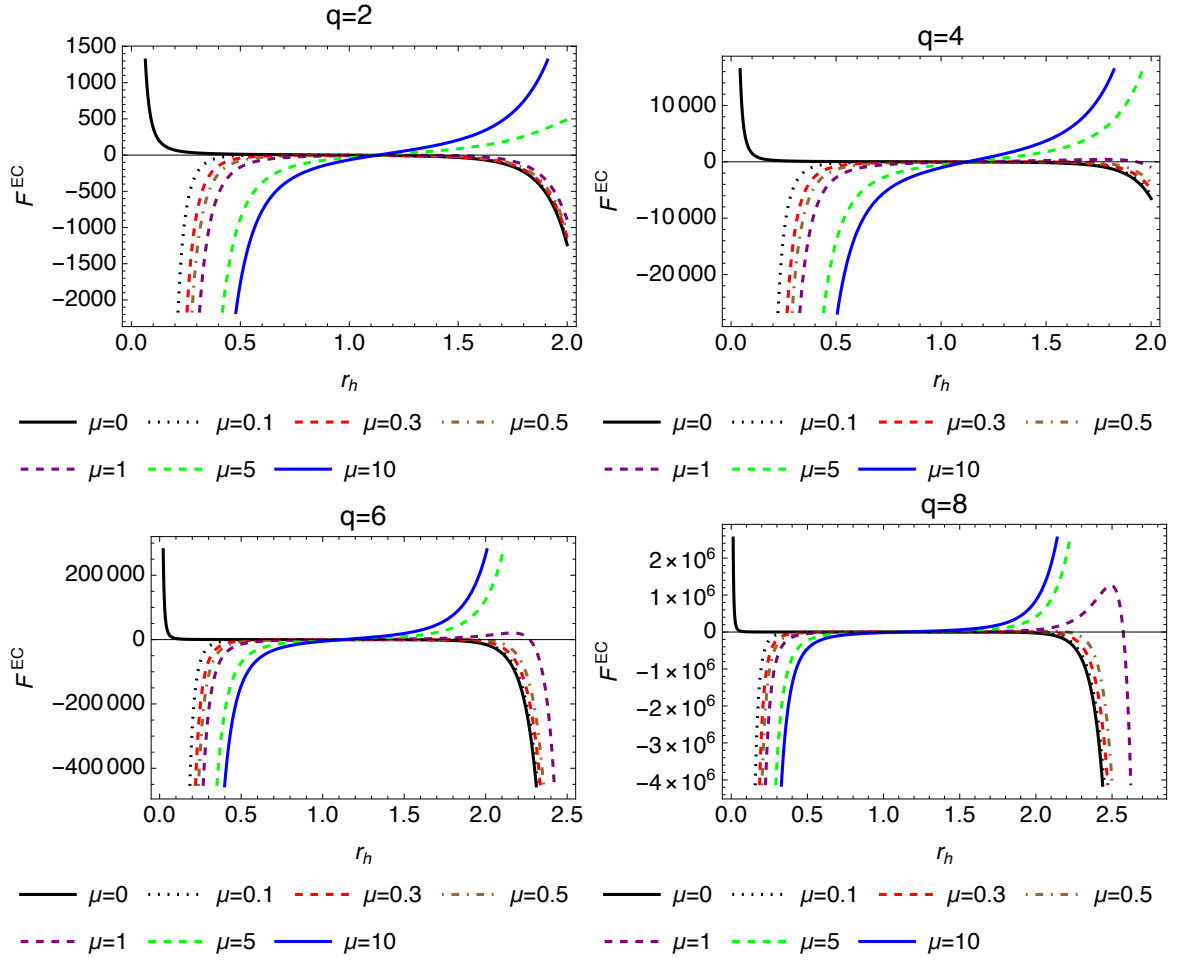


FIG. 25: Exponentially corrected Helmholtz free energy versus black hole horizon for various q and μ values.

In Fig.(25), a similar structure to the exponentially corrected internal energy is observed. Like in the previous case the functions do not coincide at a single value.

If one inserts Eq.(56) into Eq.(45), the exponentially corrected pressure can be explicitly written as

$$\begin{aligned}
 P^{EC} = \frac{1}{960\pi^2 r_h^{10}} & \left[8\pi r_h^7 \operatorname{erfi}(\sqrt{\pi} r_h) (2\pi^3 \mu q^4 - 30\pi q^2 + 15) \right. \\
 & - 147\pi \mu q^4 r_h^2 + 60\pi r_h^6 (9q^2 + r_h^2) \\
 & \left. + e^{\pi r_h^2} (60r_h^4 ((4\pi q^2 - 3) r_h^2 + 5q^2) - \mu q^4 (4\pi (4\pi^2 r_h^4 + 2\pi r_h^2 + 3) r_h^2 + 135)) \right].
 \end{aligned} \tag{57}$$

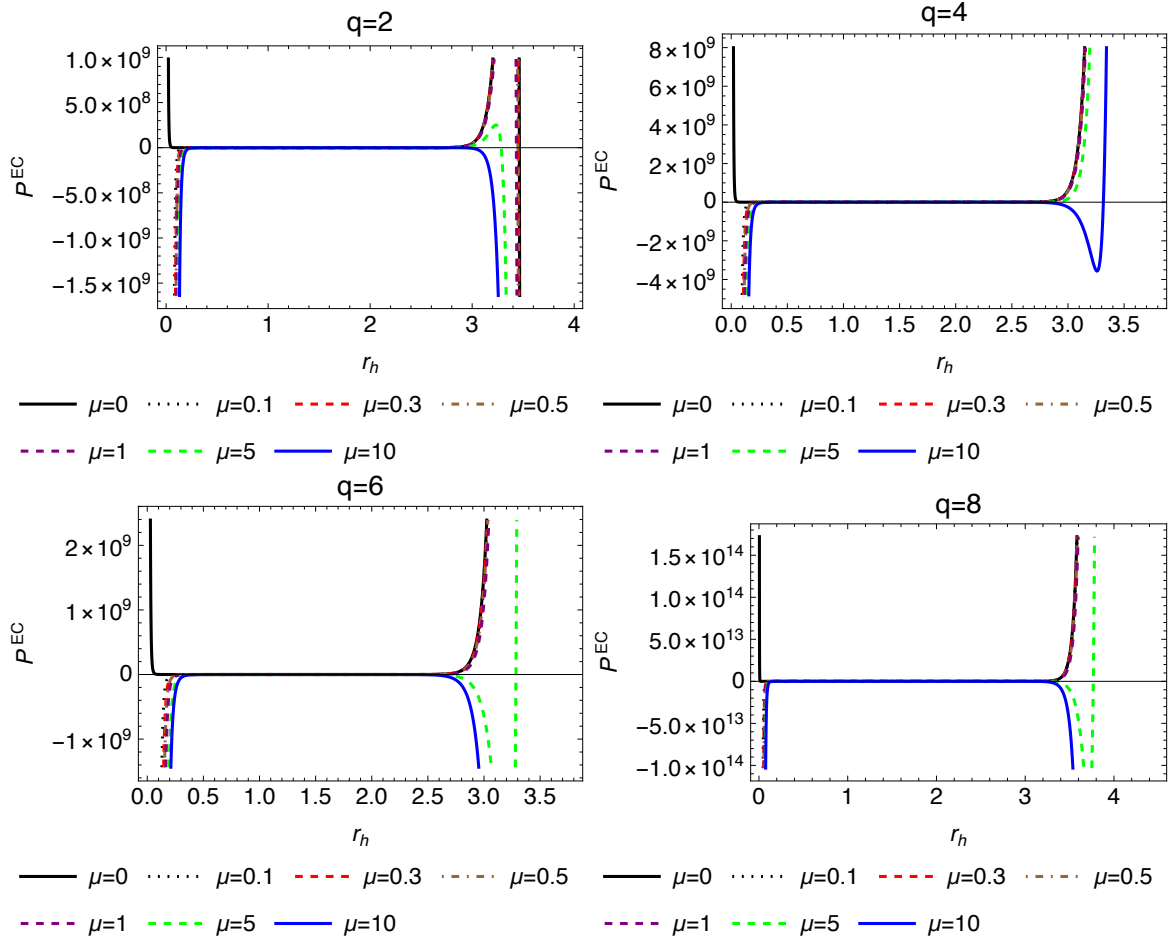


FIG. 26: Exponentially corrected pressure versus black hole horizon for various q and μ values.

Fig.(26) illustrates how the exponentially corrected pressure shifts from negative to positive values (remaining at zero for considerable r_h values) for majority of μ values. For all the cases demonstrated above, the black hole exhibits a repulsive behaviour for very small r_h , followed by an equilibrium state and switching into attractive or repulsive behaviour depending on the NED parameter.

When we put Eq.(55) and Eq.(57) into Eq.(28), the exponentially corrected enthalpy can be written as

$$\begin{aligned}
 H^{EC} = \frac{1}{144\pi r_h^7} & \left[4\pi r_h^7 \operatorname{erfi}(\sqrt{\pi} r_h) (2\pi^3 \mu q^4 - 30\pi q^2 + 15) \right. \\
 & + 3\pi r^2 (-11\mu q^4 + 60q^2 r_h^4 + 28r_h^6) \\
 & \left. - e^{\pi r_h^2} (\mu q^4 (8\pi^3 r_h^6 + 4\pi^2 r_h^4 + 6\pi r_h^2 + 27) - 60q^2 (2\pi r_h^6 + r_h^4) + 36r_h^6) \right].
 \end{aligned} \tag{58}$$

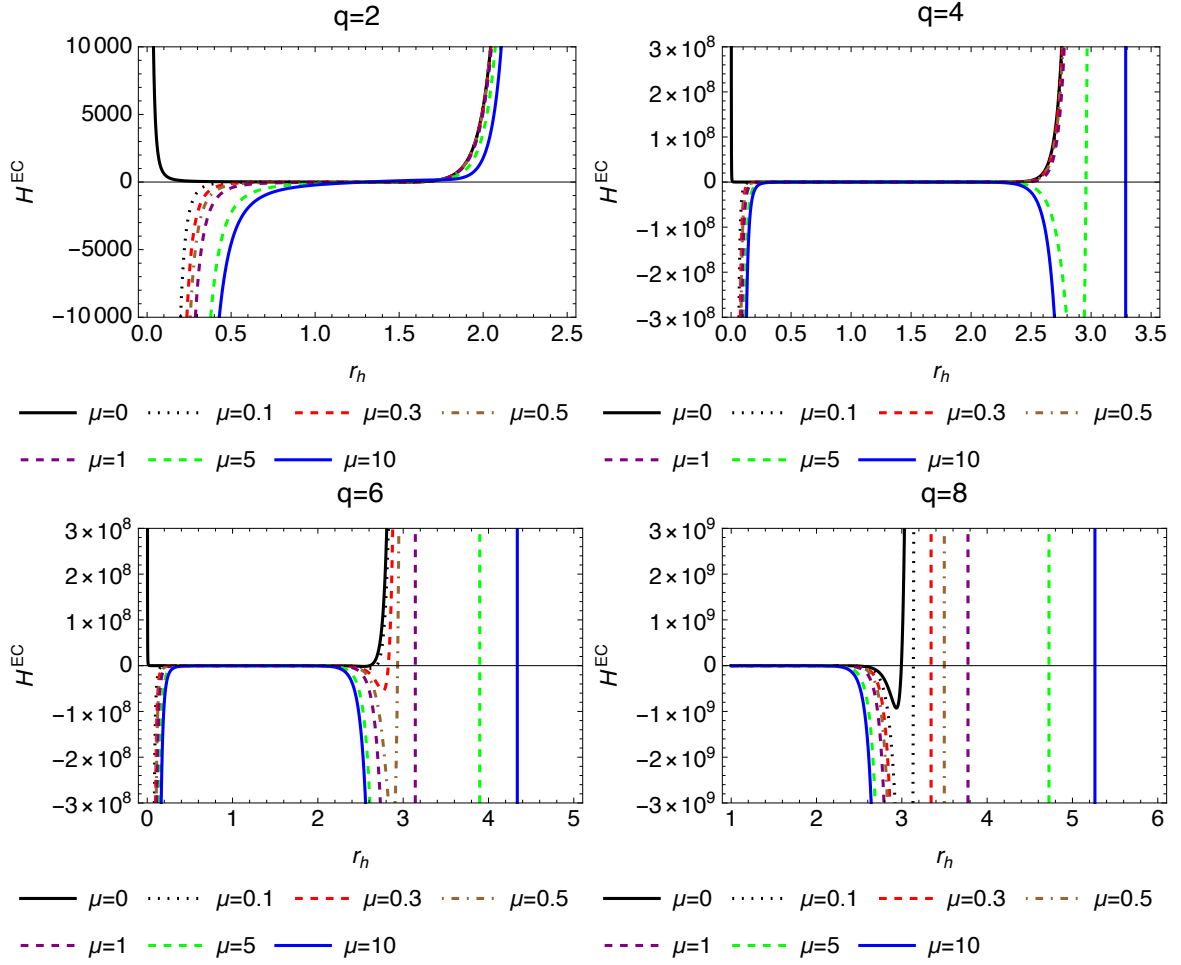


FIG. 27: Exponentially corrected enthalpy versus the black hole horizon for various q and μ values.

In the positive domain of Fig.(27), discrete vertical lines become apparent for high horizon values. One compared with the uncorrected case, the heat capacity functions for different μ values are observed to no longer converge.

One of the state functions essential for determining the global stability of the black hole is the Gibbs free energy. For an Einstein-Euler-Heisenberg black hole, the relation for Gibbs free energy can be found via

$$\begin{aligned}
 G^{EC} = \frac{1}{72\pi r_h^7} & \left[2\pi r_h^7 \operatorname{erfi}(\sqrt{\pi} r_h) (2\pi^3 \mu q^4 - 30\pi q^2 + 15) \right. \\
 & + 3\pi r_h^2 (-7\mu q^4 + 36q^2 r_h^4 + 8r_h^6) \\
 & \left. - e^{\pi r_h^2} (\mu q^4 (\pi (4\pi^2 r_h^4 + 2\pi r_h^2 + 3) r_h^2 + 18) - 12q^2 (5\pi r_h^2 + 4) r_h^4 + 36r_h^6) \right].
 \end{aligned} \tag{59}$$

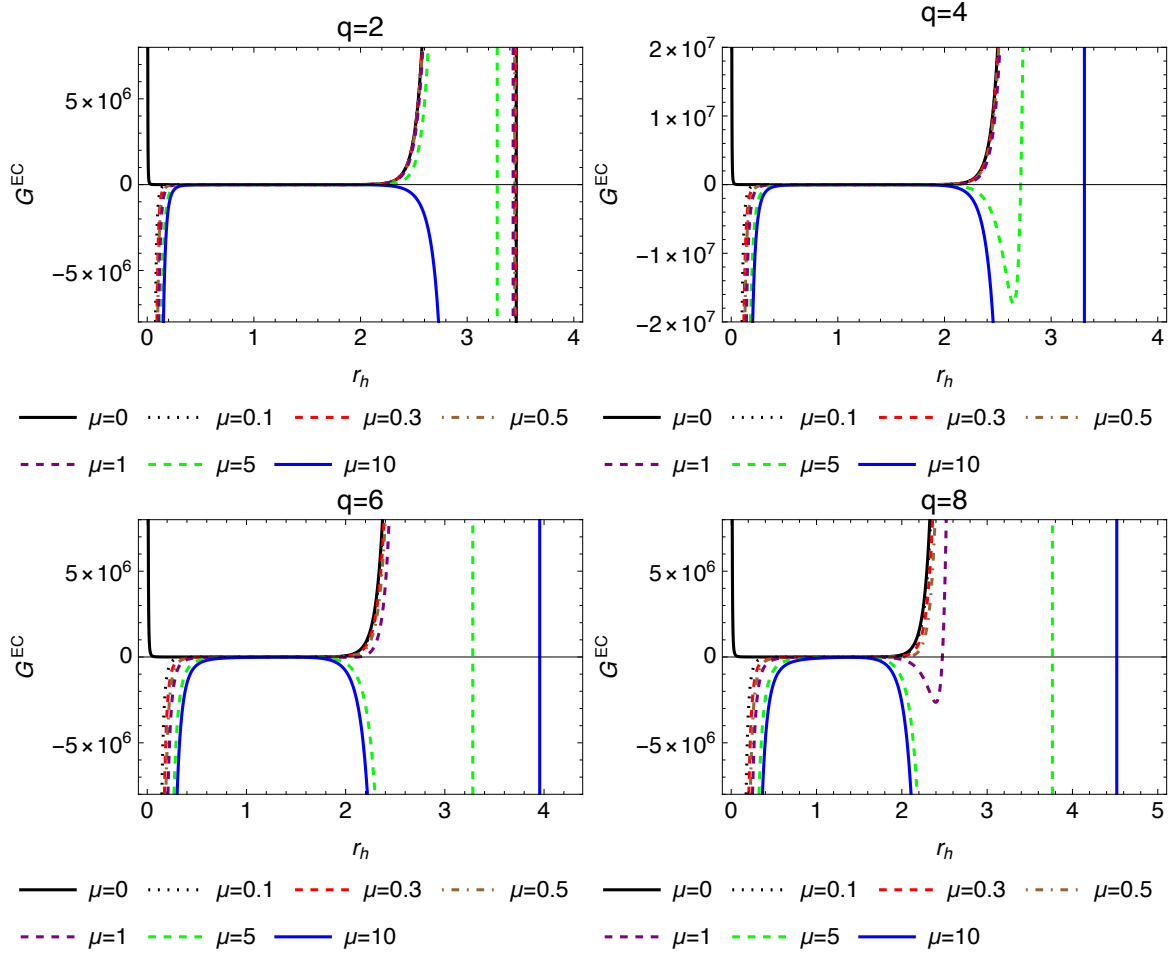


FIG. 28: Exponentially corrected Gibbs free energy versus the black hole horizon for various q and μ values.

In Fig.(28), for each specific charge and nonlinear parameter value, the exponentially corrected Gibbs free energy starts from negative values for all non-zero μ and holds a positive value after $r_h > 2$. Also, for horizon values beyond this threshold, discrete lines start appearing for all charge parameters, provided that one wishes to inspect the positive domain.

Finally, heat capacity, one of the most important thermodynamic quantities, can be examined. To see the effect of the exponential modification of heat capacity, one can put E^{EC} into Eq.(49). The exponentially corrected heat capacity then becomes

$$\begin{aligned}
 C^{EC} = \frac{16\pi r_h^2 e^{\pi r_h^2}}{7\mu q^4 - 12q^2 r_h^4 + 4r_h^6} & \left[\mu\pi q^4 r_h^2 (0.0667\pi r_h^4 + 0.0333\pi r_h^2 + 0.1333r_h^2 + 0.0833) \right. \\
 & - 0.0417\mu q^4 (4\pi r_h^4 + 2\pi r_h^2 + 3) + 0.5q^2 r_h^4 (e^{\pi r_h^2} + 1) \\
 & \left. - r_h^6 (1.0\pi q^2 + 0.5) - r_h^6 (0.0667\mu\pi^3 q^4 - q^2 + 0.5) e^{\pi r_h^2} - 0.125 \right]. \quad (60)
 \end{aligned}$$

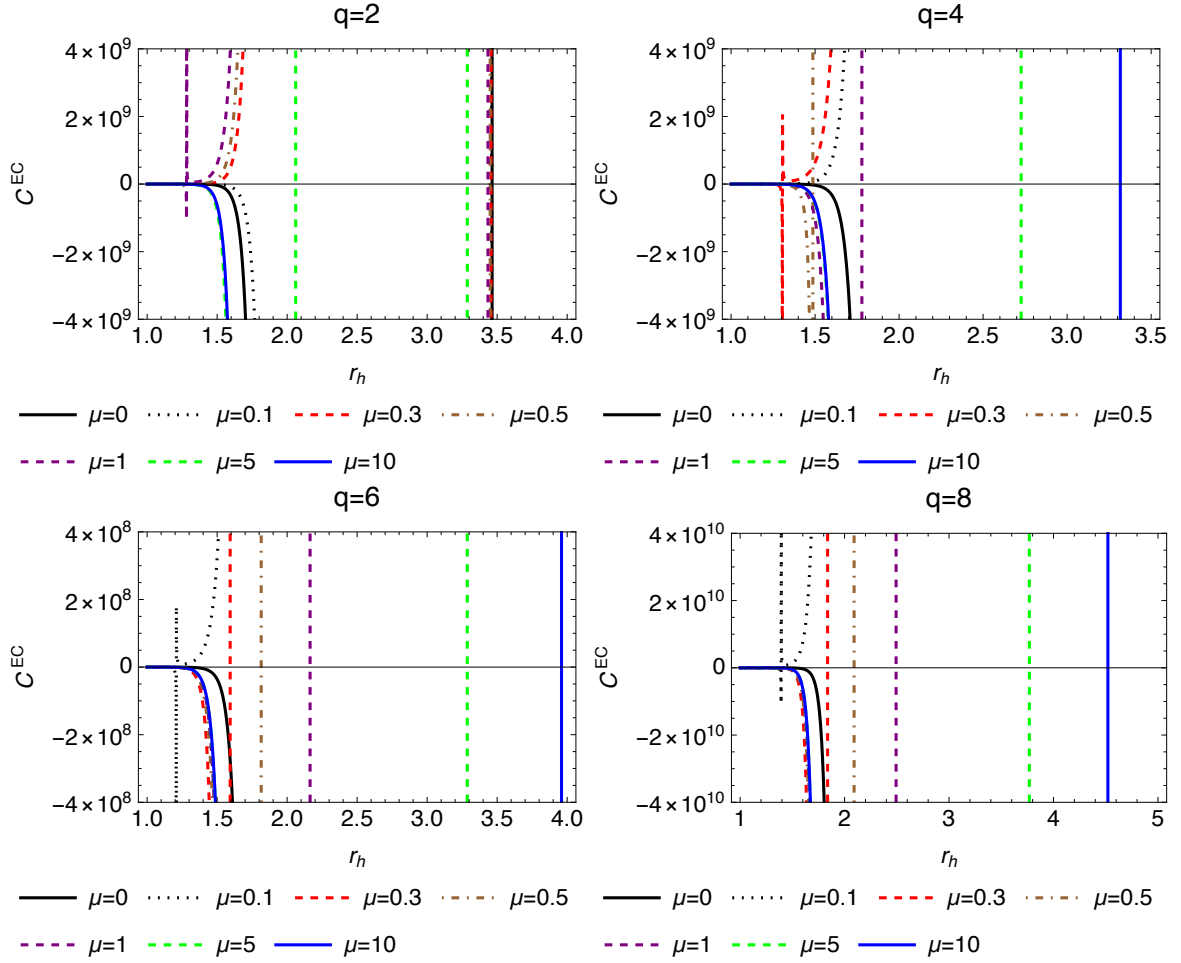


FIG. 29: Exponentially corrected stability versus the black hole horizon for various q and μ values.

The plots presented in Fig.29 represent the behaviour of C^{EC} as a function of r_h , under different q and μ parameters. For certain horizon values, the heat capacity is observed to become undefined. This might suggest thermodynamics instability and presence of potential singularities.

IV. ASTROPHYSICAL APPLICATIONS

The theory of NED finds numerous applications in the field of astrophysics, as the universe is filled with sources of strong electromagnetic field. As examples, one can consider neutron stars and magnetars, since both hold the ability of producing magnetic field whose magnitude can reach up to $10^6 - 10^9$ T [77]. In this regard, one can look for the observational implications of the theoretical discussions covered so far with the aid of two key astrophysical phenomena: the gravitational lensing and the gravitational redshift.

A. Gravitational Lensing around Einstein-Euler-Heisenberg Black Holes

In the standard Euclidean geometry, the inner product of two distinct vectors gives us the invariant angle in between. Rindler and Ishak extended this geometric result to curved spacetimes, developing a methodology for calculating the deflection of the relativistic light [65]. For the lensing formulation developed by RI, the geometry diagrammed below, which features a massive object at its center, is considered.

Thus, $\epsilon = \psi - \varphi$ can measure the one-sided bending angle of the curved spacetime. When metric (7) is substituted in Eq. (66), the null geodesic equation of Euler-Heisenberg spacetime takes the form

$$\frac{d^2 u}{d\varphi^2} + u = 3Mu^2 - 2q^2 u^3 + \frac{\mu q^4}{5} u^7 \quad (69)$$

Now, the solution of Eq.(69) can be analysed. Since finding the exact solution of such a nonlinear differential equation is rather challenging, the standard approximate solution method can be used to obtain a perturbative solution of Eq. (69). In this context, substituting $u(\varphi) = \sin(\varphi)/R$, the linear and homogeneous solution of Eq. (69), into the nonlinear part on the right-hand side of Eq. (69), the first-order approximate solution becomes

$$u = \frac{1}{r} = \frac{\sin \varphi}{R} + \frac{M}{R^2} (1 + \cos^2 \varphi) + \frac{3q^2}{R^3} \left(\frac{\varphi \cos \varphi}{4} - \frac{\cos^2 \varphi \sin \varphi}{12} - \frac{\sin \varphi}{6} \right) + \frac{\mu q^4}{40R^7} \left(\sin \varphi - \frac{35\varphi}{16} - \frac{19 \cos^4 \varphi \sin \varphi}{24} + \frac{29 \cos^2 \varphi \sin \varphi}{16} \right). \quad (70)$$

The first-order derivative of $r(\varphi)$ with respect to φ becomes ,

$$\frac{dr}{d\varphi} = r^2 \left[-\frac{\cos \varphi}{R} + \frac{q^2}{4R^3} (3\varphi \sin \varphi - \cos \varphi - \sin 2\varphi \sin \varphi + \cos^3 \varphi) + \frac{M \sin 2\varphi}{R^2} + \frac{\mu q^4}{40R^7} \left(\frac{35}{16} - \cos \varphi - \frac{19 \cos \varphi \sin^2 2\varphi}{24} + \frac{29 \sin 2\varphi \sin \varphi}{16} \right) \right]. \quad (71)$$

Note that in Eqs. (70) and (71) the integration parameter is called the impact parameter which is generally large ($R \gg 1$). Additionally, taking $\varphi = \pi/2$ in Eq.(70), the closest approach distance is found as

$$u(\varphi = \pi/2) = \frac{1}{r_0} = \frac{1}{R} + \frac{M}{R^2} - \frac{q^2}{2R^3} + \frac{\mu q^4 (32 - 35\pi)}{1280R^7}. \quad (72)$$

Now, the small angle ψ_0 can be calculated by setting $\varphi = 0$. In this case, from Eq.(70) and Eq.(71), one can write

$$r(\varphi = 0) \approx \frac{R^2}{2M}, \quad \mathcal{A}(r, \varphi = 0) \approx -\frac{r^2}{R}. \quad (73)$$

Once all the information is plugged into the Rindler-Ishak lensing formula using small angle approximation ($\tan(\psi_0) \approx \psi_0$), Eq.(68) gives

$$\begin{aligned} \epsilon &\simeq \frac{2M}{R} [g^{rr}]^{\frac{1}{2}} \simeq \frac{2M}{R} \left(1 - \frac{4M^2}{R^2} + \frac{4M^2 q^2}{R^4} - \frac{16\mu q^4 M^6}{5R^{12}} \right)^{\frac{1}{2}} \\ &\simeq \frac{2M}{R} \left(1 - \frac{2M^2}{R^2} + \frac{2M^2 q^2}{R^4} - \frac{8\mu q^4 M^6}{5R^{12}} \right) + \mathcal{O} \left(\frac{M^{13} \mu^2 q^8}{R^{25}} \right). \end{aligned} \quad (74)$$

B. Gravitational Redshift around Einstein-Euler-Heisenberg Black Holes

Another significant observational phenomenon known as gravitational redshift, which is observable in an area with lesser gravitational field, is caused by light or other electromagnetic radiation emitted from a source in a strong gravitational field shifting to longer wavelengths. This phenomena is predicted by general relativity. The gravitational redshift analysis in references [78] and [79] describe the spacetime geometry surrounding a non-rotating black hole. This approach indicates that the formula for the gravitational redshift can be expressed as

$$z = \frac{\lambda_o - \lambda_e}{\lambda_e} = \frac{\lambda_o}{\lambda_e} - 1 = \frac{\omega_o}{\omega_e} - 1, \quad (75)$$

where

$$\frac{\omega_e}{\omega_o} = \sqrt{g_{tt}}. \quad (76)$$

Here, λ_e and λ_o represent the emitted and the observed wavelengths, respectively, whereas g_{tt} corresponds to the $-tt$ component of the relevant metric tensor. Similarly, ω_e and ω_o denote the emitted and the observed frequencies. When we put Eq.(7) into Eq.(75), the gravitational redshift of the Einstein-Euler-Heisenberg black Hole becomes

$$z = \frac{M}{R} - \frac{q^2}{2R^2} + \frac{\mu q^4}{40R^6}. \quad (77)$$

C. Astrophysical Applications: Strong Electrically Charged Compact Stars

In the light of the information obtained, the relevant astrophysical applications are discussed. In this purpose, the numerical analysis has been established for three realistic charged compact stars, with their properties detailed in Table-1.

TABLE I: The numerical values of the mass, radius and charge of three compact stars. Here, M_\odot represents the mass of the Sun[64].

Charged Compact Stars	M	Radius (km)	Electric Charge (C)
Vela X-1	$1.77M_\odot$	9.56	1.81×10^{20}
SAXJ 1808.4-3658	$1.435M_\odot$	7.07	1.87×10^{20}
4U 1820-30	$2.25M_\odot$	10	1.89×10^{20}

Note that in the numerical analyses to be performed using Eq.(74) and Eq.(77) obtained in standard geometric units, we should use the factors Gc^{-2} (M) and $G^{1/2}c^{-2}(4\pi\epsilon_0)^{-1/2}$ for charge the mass (M) and the electric charge (q), respectively, based on the values provided in Table-1. Here, $G = 6.67408 \times 10^{-11}m^3kg^{-1}s^{-2}$ represents the gravitational constant, $c = 3 \times 10^8ms^{-1}$ denotes the speed of light and $\epsilon_0 = 8.85418 \times 10^{-12}C^2N^{-1}m^2$ is the vacuum permittivity. Note that all the resulting graphical analyses will be in SI units, and for all the cases, the boundary condition $\mu/M^2 \leq 50/81$ will be applied as a fundamental constraint. Accordingly, all numerical evaluations will be performed by adopting the upper limit, leading to the condition $\mu = 50M^2/81$. This approach ensures that the analyses consistently operate within the specified parameter space, facilitating a systematic investigation of the nonlinear effects while maintaining adherence to the imposed boundary constraints. Additionally, it should be noted that this choice allows for the consideration of the maximum nonlinear effects. Also note that the boundary condition derived from the solution $q^2/M^2 \leq 25/24$ is satisfied for the numerical values corresponding to the compact objects under consideration. This condition ensures consistency with the physical and mathematical framework applied to model such compact astrophysical structures.

Fig.(31) illustrates the one-sided bending angle for three electrically charged compact objects: Vela X-1, SAXJ1808.4-3658, and 4U1820-30. As evident from Fig.(31), the presence of electric charge significantly influences the bending angle of light.

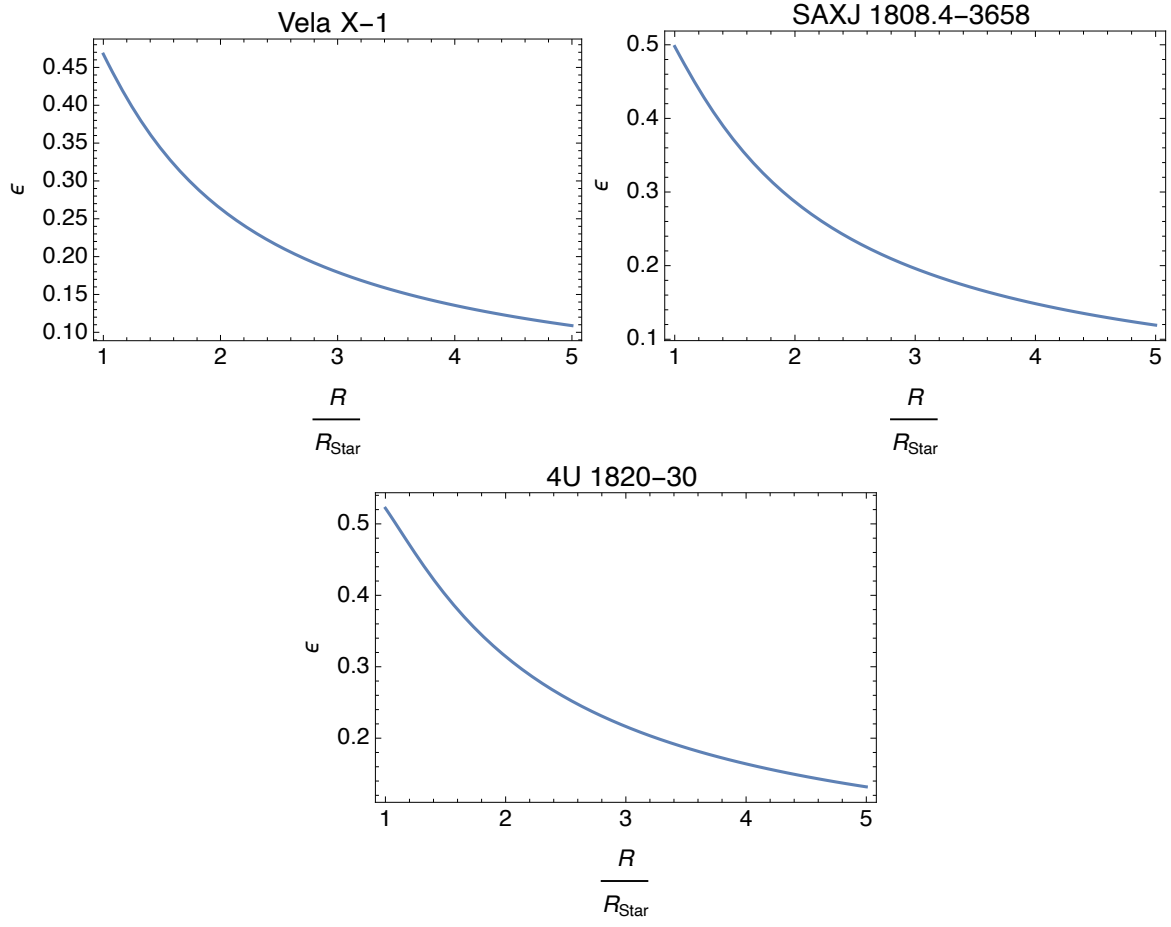


FIG. 31: The plots of deflection angle ϵ versus R/R_{star} for each compact objects in Table 1.

Fig.(32) presents the gravitational redshifts, plotted individually for each compact object.

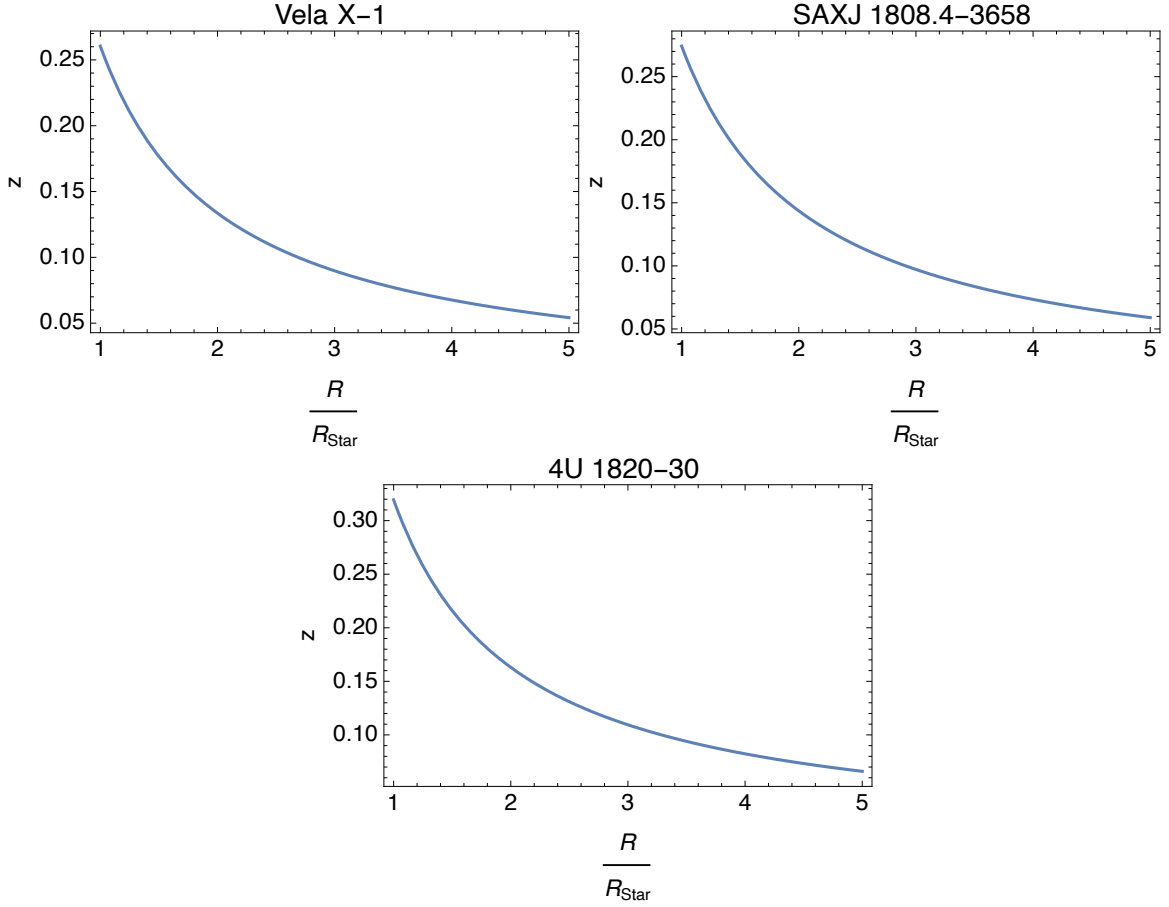


FIG. 32: The plots show the variation of the gravitational redshift with respect to R/R_{star} for each compact object listed in Table 1.

V. CONCLUSION

In this study, the nonlinear Euler-Heisenberg theory has been investigated from the perspectives of the general theory of relativity and astrophysics. We have initiated our discussions by applying logarithmic and exponential corrections to the classical Hawking-Bekenstein entropy and then checked for the consequent effects arising due to these modifications mainly via the inspection of the graphical illustrations. The concerned graphs have been obtained based on the detailed analytical evaluations of the thermodynamic parameters of the Einstein-Euler-Heisenberg black hole. The comparisons of the uncorrected and logarithmically corrected Helmholtz free energy and pressure against horizon graphs have revealed interesting information regarding the properties of the concerned black hole. Firstly, the general behaviour of the corrected functions are found to act as the reflections of the uncorrected ones through the x -axis. Furthermore, recalling that the logarithmic corrections arise due to small fluctuations around the equilibrium, we suggest that such corrections incorporate information regarding the interaction of the Einstein-Euler-Heisenberg black hole with vacuum. Accordingly, in Fig 16, the effect of vacuum fluctuations are observed to become apparent, especially for large charge and NED parameter values. In other words, as the nonlinear effects become dominant, making further comments on the corrections due to vacuum polarisation gets relatively easier.

On the other hand, the logarithmic corrections have not seem to have caused any significant change in the overall classical thermodynamic behaviour of the black hole, whereas in the exponential case, the graphs of the associated quantities have been found to behave in a completely different manner. For instance, in the positive domain of the heat capacity versus horizon graphs, the non-perturbative quantum corrections have been observed to introduce discrete vertical lines for all values of q . The strikingly different patterns evident in all exponentially corrected thermodynamic graphs make it tempting to suggest that the dominance of quantum effects might be the underlying reason behind the revelation of such a discrete behaviour. In a similar context, this behaviour might suggest the forbiddance of certain states within certain horizon values, i.e. the quantisation of the thermodynamic states of the

Einstein-Euler-Heisenberg black hole.

Based on the associated plots, we have seen that to distinguish the differences between the effect of the logarithmic and exponential corrections on the thermodynamic states of the Einstein-Euler-Heisenberg black hole, one could check the behaviour of the Helmholtz free energy versus black hole horizon for various q and μ values. When $r_h < 1$, the logarithmically corrected Helmholtz free energy function behaves in the exact opposite manner as the uncorrected and the exponentially corrected ones. Thus, we suggest the exponential corrections do not reveal the details related to variations arising due to vacuum fluctuations. On the other hand, for $r_h > 1$, the uncorrected and the logarithmically corrected Helmholtz free energy function converge for all q and μ values, whereas the exponentially corrected ones diverge from one another.

In addition to the investigation of the thermodynamic quantities via the Smarr formula, we have estimated the one-sided bending angle and the gravitational redshift of electromagnetic radiation in the vicinity of astronomical structures obeying the nonlinear Euler-Heisenberg model. We believe that this study sheds light on the influence of the logarithmic and the exponential corrections on entropy, which are both crucial when it comes to the determination of the complete form of entropy to be used in black hole thermodynamics and any relevant application.

-
- [1] J. C. Maxwell, Philosophical transactions of the Royal Society of London pp. 459–512 (1865).
 - [2] F. Sauter, Zeitschrift für Physik **69**, 742 (1931).
 - [3] J. Schwinger, Physical Review **82**, 664 (1951).
 - [4] P. A. M. Dirac, Proceedings of the Royal Society of London. Series A, Containing Papers of a Mathematical and Physical Character **117**, 610 (1928).
 - [5] M. Born and L. Infeld, Proceedings of the Royal Society of London. Series A, Containing Papers of a Mathematical and Physical Character **144**, 425 (1934).
 - [6] A. García D, H. Salazar I, and J. Plebański, Il Nuovo Cimento B (1971-1996) **84**, 65 (1984).
 - [7] E. Fradkin and A. A. Tseytlin, Physics Letters B **163**, 123 (1985).
 - [8] H. Salazar I, A. García D, and J. Plebański, Journal of mathematical physics **28**, 2171 (1987).
 - [9] G. Gibbons and D. Rasheed, Nuclear Physics B **454**, 185 (1995).
 - [10] S. Deser and G. Gibbons, Classical and Quantum Gravity **15**, L35 (1998).
 - [11] E. Ayon-Beato and A. Garcia, Physical review letters **80**, 5056 (1998).
 - [12] W. Heisenberg and H. Euler, Z. Phys. **98**, 714 (1936), physics/0605038.
 - [13] H. J. Mosquera Cuesta and J. M. Salim, Monthly Notices of the Royal Astronomical Society **354**, L55 (2004).
 - [14] J. Y. Kim and T. Lee, Journal of Cosmology and Astroparticle Physics **2011**, 017 (2011).
 - [15] N. Breton and L. López, Physical Review D **104**, 024064 (2021).
 - [16] D. Magos and N. Breton, Physical Review D **102**, 084011 (2020).
 - [17] A. Bermúdez Manjarres, M. Nowakowski, and D. Batic, International Journal of Modern Physics A **35**, 2050211 (2020).
 - [18] A. Lindner, B. Ölmez, and H. Ruhl, Journal of Computational Physics: X **17**, 100124 (2023).
 - [19] S. Kruglov, Modern Physics Letters A **32**, 1750092 (2017).
 - [20] J. W. York Jr, Physical Review D **33**, 2092 (1986).
 - [21] R. C. Myers and J. Z. Simon, Physical Review D **38**, 2434 (1988).
 - [22] B. P. Dolan, Classical and Quantum Gravity **28**, 235017 (2011).
 - [23] A. Anabalón, M. Appels, R. Gregory, D. Kubizňák, R. B. Mann, and A. Övgün, Physical Review D **98**, 104038 (2018).
 - [24] J. D. Bekenstein, in *JACOB BEKENSTEIN: The Conservative Revolutionary* (World Scientific, 2020), pp. 303–306.
 - [25] J. D. Bekenstein, Physical Review D **7**, 2333 (1973).
 - [26] S. W. Hawking, Communications in mathematical physics **43**, 199 (1975).
 - [27] S. W. Hawking, Nature **248**, 30 (1974).
 - [28] S. W. Hawking, Physical Review D **14**, 2460 (1976).
 - [29] R. Penrose, in *General relativity* (1979).
 - [30] S. W. Hawking and D. N. Page, Communications in Mathematical Physics **87**, 577 (1983).
 - [31] W. Greiner, L. Neise, and H. Stöcker, *Thermodynamics and statistical mechanics* (Springer Science & Business Media, 2012).
 - [32] A. Strominger and C. Vafa, Physics Letters B **379**, 99 (1996).
 - [33] S. Das, P. Majumdar, and R. K. Bhaduri, Classical and Quantum Gravity **19**, 2355 (2002).
 - [34] J. Alsing, B. Wandelt, and S. Feeney, Monthly Notices of the Royal Astronomical Society **477**, 2874 (2018).
 - [35] S. Mahapatra, P. Phukon, and T. Sarkar, Physical Review D—Particles, Fields, Gravitation, and Cosmology **84**, 044041 (2011).
 - [36] B. Pourhassan, H. Farahani, F. Kazemian, İ. Sakallı, S. Upadhyay, and D. V. Singh, Physics of the Dark Universe **44**, 101444 (2024).
 - [37] M. Dehghani and B. Pourhassan, Modern Physics Letters A **36**, 2150158 (2021).

- [38] A. Dabholkar, J. Gomes, and S. Murthy, *Journal of High Energy Physics* **2015**, 1 (2015).
- [39] S. N. Solodukhin, *Physical Review D* **57**, 2410 (1998).
- [40] H. A. Kastrup, *Phys. Lett. B* **413**, 267 (1997), gr-qc/9707009.
- [41] R. B. Mann and S. N. Solodukhin, *Nuclear Physics B* **523**, 293 (1998).
- [42] A. Medved and G. Kunstatler, *Physical Review D* **60**, 104029 (1999).
- [43] R. K. Kaul and P. Majumdar, *Physical Review Letters* **84**, 5255 (2000).
- [44] A. Medved and G. Kunstatler, *Physical Review D* **63**, 104005 (2001).
- [45] G. Gour and A. Medved, *Classical and Quantum Gravity* **20**, 3307 (2003).
- [46] A. Chatterjee and P. Majumdar, *Physical Review Letters* **92**, 141301 (2004).
- [47] C. Rovelli, *Physical Review Letters* **77**, 3288 (1996).
- [48] M. Domagala and J. Lewandowski, *Classical and Quantum Gravity* **21**, 5233 (2004).
- [49] A. Medved, *Classical and Quantum Gravity* **22**, 133 (2004).
- [50] E. Berti, A. Buonanno, and C. M. Will, *Physical Review D—Particles, Fields, Gravitation, and Cosmology* **71**, 084025 (2005).
- [51] A. Medved and E. C. Vagenas, *Modern Physics Letters A* **20**, 1723 (2005).
- [52] J. Zhang, *Physics Letters B* **668**, 353 (2008).
- [53] L. V. Iliesiu, S. Murthy, and G. J. Turiaci, arXiv preprint arXiv:2209.13608 (2022).
- [54] A. Chatterjee and A. Ghosh, *Physical Review Letters* **125**, 041302 (2020).
- [55] B. Pourhassan and M. Faizal, *Europhysics Letters* **111**, 40006 (2015).
- [56] B. Pourhassan, S. Upadhyay, H. Saadat, and H. Farahani, *Nuclear Physics B* **928**, 415 (2018).
- [57] B. Pourhassan and M. Faizal, *Nuclear Physics B* **913**, 834 (2016).
- [58] R. Ali, R. Babar, Z. Akhtar, and A. Övgün, *Results in Physics* **46**, 106300 (2023).
- [59] M. Mangut, Ö. Gürtuğ, and İ. Sakallı, *Physica Scripta* **99**, 055005 (2024).
- [60] M. Zhang, *Nuclear Physics B* **935**, 170 (2018).
- [61] M. A. de Paula, H. C. L. Junior, P. V. Cunha, and L. C. Crispino, *Physical Review D* **108**, 084029 (2023).
- [62] W. Javed, A. Hamza, and A. Övgün, *Physical Review D* **101**, 103521 (2020).
- [63] Q.-M. Fu, L. Zhao, and Y.-X. Liu, *Physical Review D* **104**, 024033 (2021).
- [64] O. Gurtug and M. Mangut, *Physical Review D* **99**, 084003 (2019).
- [65] W. Rindler and M. Ishak, *Physical Review D—Particles, Fields, Gravitation, and Cosmology* **76**, 043006 (2007).
- [66] O. Gurtug and M. Mangut, *Annalen der Physik* **532**, 1900576 (2020).
- [67] M. Ilyas, *The European Physical Journal C* **78**, 757 (2018).
- [68] O. Gurtug, M. Mangut, and M. Halilsoy, *Astroparticle Physics* **128**, 102558 (2021).
- [69] M. Mangut, H. Gürsel, S. Kanzi, and İ. Sakallı, *Universe* **9**, 225 (2023).
- [70] M. Mangut, H. Gürsel, and İ. Sakallı, *Astroparticle Physics* **144**, 102763 (2023).
- [71] D. Amaro and A. Macías, *Physical Review D* **102**, 104054 (2020).
- [72] M. Cvetič and D. Youm, *Physical Review D* **54**, 2612 (1996).
- [73] B. Toshmatov, Z. Stuchlík, and B. Ahmedov, *The European Physical Journal Plus* **132**, 1 (2017).
- [74] A. L. Wasserman, *Thermal physics: concepts and practice* (Cambridge University Press, 2011).
- [75] G. W. Gibbons and S. W. Hawking, *Physical Review D* **15**, 2752 (1977).
- [76] M. Faizal and B. Pourhassan, *Physics Letters B* **751**, 487 (2015).
- [77] N. Breton, C. Lämmerzahl, and A. Macías, *Physical Review D* **107**, 064026 (2023).
- [78] N. K. Glendenning, *Compact stars: Nuclear physics, particle physics and general relativity* (Springer Science & Business Media, 2012).
- [79] O. Zubairi, A. Romero, and F. Weber, in *Journal of Physics: Conference Series* (IOP Publishing, 2015), vol. 615, p. 012003.